UNIVERSIDADE FEDERAL DO CEARÁ
CENTRO DE TECNOLOGIA
DEPARTAMENTO DE ENGENHARIA QUÍMICA
PROGRAMA DE PÓS-GRADUAÇÃO EM EMGENHARIA QUÍMICA

RAFAEL AUGUSTO MORALES OSPINO

ASSESSMENT OF TEMPERATURE SWING ADSORPTION CONFIGURATIONS FOR CO_2 CAPTURE ON ZEOLITE 13X

FORTALEZA

2018

RAFAEL AUGUSTO MORALES OSPINO

ASSESSMENT OF TEMPERATURE SWING ADSORPTION CONFIGURATIONS FOR CO_2 CAPTURE ON ZEOLITE 13X

Dissertação apresentada ao Programa de Pós-Graduação em Engenharia Química da Universidade Federal do Ceará, como parte dos requisitos para obtenção do Título de Mestre em Engenharia Química. Área de Concentração: Processos Químicos e Bioquímicos.

Orientador: Prof. Dr. Moisés Bastos Neto
Coorientadora: Profª. Drª. Diana Cristina Silva de Azevedo

FORTALEZA

2018

Dados Internacionais de Catalogação na Publicação
Universidade Federal do Ceará
Biblioteca Universitária
Gerada automaticamente pelo módulo Catalog, mediante os dados fornecidos pelo(a) autor(a)

O1a Ospino, Rafael Augusto Morales.
Assessment of Temperature Swing Adsorption configurations for CO2 capture on zeolite 13X / Rafael Augusto Morales Ospino. – 2018.
100 f. : il. color.

Dissertação (mestrado) – Universidade Federal do Ceará, Centro de Tecnologia, Programa de Pós-Graduação em Engenharia Química, Fortaleza, 2018.
Orientação: Prof. Dr. Moisés Bastos Neto.
Coorientação: Profa. Dra. Diana Cristina Silva De Azevedo.

1. TSA. 2. CO2 . 3. Zeolite 13X.. I. Título.

CDD 660

RAFAEL AUGUSTO MORALES OSPINO

ASSESSMENT OF TEMPERATURE SWING ADSORPTION CONFIGURATIONS FOR CO_2 CAPTURE ON ZEOLITE 13X

Dissertation submitted to Universidade Federal do Ceará as a requirement to obtain the Master's Degree in Chemical Engineering.
Concentration area: Chemical and biological separation processes.

Approved on 21 February 2018.

_____

Prof. Dr. Moisés Bastos Neto
Universidade Federal do Ceará (UFC)

_____

Prof. Dr. Enrique Vilarrasa García
Universidade Federal do Ceará (UFC)

_____

Prof. Dr. Sebastião Mardônio Pereira de Lucena
Universidade Federal do Ceará (UFC)

_____

Prof. Dr. Amaro Gomes Barreto Júnior
Universidade Federal do Rio de Janeiro (UFRJ)

RESUMO

Neste estudo, foram avaliadas duas configurações de Adsorção com Modulação na Temperatura (TSA) com o objetivo de avaliar sua eficácia na captura de CO_2 no adsorvente comercial zeólita 13X dentro de um cenário de pós-combustão. Uma unidade de laboratório de leito fixo, com uma única coluna, foi empregada para obter curvas de ruptura experimentais (adsorção) e os perfis de depleção subsequentes (dessorção). Considerando uma corrente seca e dessulfurada de gases de combustão, as curvas de ruptura para CO_2-N_2 (15/75% v/v) em Hélio foram realizadas a 25, 50 e 75 °C. A etapa de dessorção foi realizada seguindo duas estratégias de regeneração de TSA: a primeira consiste em uma fase de purga seguida de uma fase de purga junto com aquecimento (*configuração 1*) e, a segunda, envolvendo apenas a fase de purga com aquecimento (*configuração 2*). Também foram obtidas isotermas de equilíbrio de adsorção para CO_2 e N_2 puros nas mesmas temperaturas dos testes dinâmicos, na faixa de 0 a 10 bar. Finalmente, uma formulação de modelo matemático considerando a modelagem das isotermas de equilíbrio e os balanços de fenômenos de transporte foi realizada para prever todo o perfil de adsorção-dessorção. Os resultados obtidos nas curvas de ruptura mostraram que a separação de CO_2 em N_2 na zeólita 13X é atingida pelo processo de adsorção nas condições estudadas com uma preferência significativa para o CO_2. No que diz respeito à fase de dessorção, a *configuração 1* pode não ser adequada para a integração das etapas de adsorção-dessorção, uma vez que apenas a fase de purga duplica o tempo da etapa de adsorção. Por outro lado, a *configuração 2* é susceptível de sincronizar todo o processo de adsorção-dessorção, dado que o tempo de regeneração foi significativamente reduzido por esta estratégia. No entanto, a *configuração 1* conseguiu obter uma recuperação total do CO_2 previamente adsorvido, com todas as temperaturas testadas durante a etapa de aquecimento, enquanto a *configuração 2*, atingiu valores de recuperação em torno de 92%. Temperaturas moderadas (por exemplo, 125-150 °C) são sugeridas a serem usadas para a estratégia de regeneração da *configuração 2* para assim evitar altos custos de energia na fase de aquecimento. As simulações foram capazes de reproduzir bem as curvas de ruptura experimentais; no entanto, para os perfis de dessorção, observaram-se algumas discrepâncias.

Palavras-chave: TSA. CO_2. Zeólita 13X.

ABSTRACT

In this study, two configurations of Temperature Swing Adsorption (TSA) were assessed with the aim of evaluating their efficacy on CO_2 capture on commercial adsorbent zeolite 13X within a post-combustion scenario. A Fixed Bed Laboratory Unit (FBU) with a single column was employed to obtain experimentally breakthrough curves (adsorption) and the subsequent depletion profiles (desorption). Considering a dry desulfurized flue gas stream, breakthrough curves for CO_2-N_2 (15/75 % v/v) in Helium were performed at 25, 50 and 75 °C. The desorption step was accomplished following two TSA regeneration strategies: a two phase desorption arrangement (*configuration 1*) consisting of a purging phase and then a heating-purging phase, and a one phase desorption arrangement (*configuration 2*) involving only the heating-purging phase. Adsorption equilibrium isotherms were also obtained for pure CO_2 and N_2 on zeolite 13X at the same temperatures of the dynamic tests in the range of 0-10 bar. Finally, a mathematical model formulation, considering isotherm modeling and transport phenomena balances, was performed to predict the whole adsorption-desorption profile. The results obtained on breakthrough curves showed that CO_2 separation from N_2 on zeolite 13X is accomplished by adsorption under the studied conditions with a meaningful preference on CO_2. In regard with the desorption phase, *configuration* 1 may not be proper for an integration of adsorption-desorption steps once only the purge phase duplicates the time of the adsorption stage. On the other hand, *configuration 2* is likely to synchronize the whole adsorption –desorption process since the regeneration time was significantly reduced by this strategy. However, *configuration 1* managed to obtain full CO_2 recovery with all the temperatures tested during the heating step, whereas *configuration 2* reached recovery values around 92 %. Moderate temperatures (e.g. 125-150 °C) are encouraged to be used for *configuration 2* regeneration strategy to avoid energy penalties. Simulations were able to reproduce well the experimental breakthrough curves, however for the desorption profiles, some discrepancies were observed.

Keywords: TSA. CO_2. Zeolite 13X.

LIST OF FIGURES

Figure 1 - Classification of physisorption isotherms 20

Figure 2 - Schematics of adsorption, carbon capture process in a cylindrical bed. 23

Figure 3 - Types of separation by adsorption: A) equilibrium, (B) kinetic, or (C) molecular sieving mechanisms. Large balls represent N_2 molecules and small ones CO_2. 24

Figure 4 - Diversity of zeolite structures 26

Figure 5 - Monocomponent Breakthrough Curve. 28

Figure 6 - Breakthrough curve (normalized eluent concentration, C_i/C_{io} vs time). 29

Figure 7 - Multicomponent Breakthrough Curve. 29

Figure 8 - Schematic representation of PSA and TSA. 30

Figure 9 - Basic scheme of Autosorb IQ3 (Quantachrome, USA). 35

Figure 10- Fixed Bed Laboratory Unit (FBU) 40

Figure 11- Experiment outline sequence. 42

Figure 12- Normalized concentration profile for CO_2 and N_2 in adsorption/desorption process. Regeneration by He purge + (Temperature swing + He purge). 43

Figure 13- Normalized concentration profile for CO_2 and N_2 in adsorption and desorption process. Regeneration by (Temperature swing + He purge). 43

Figure 14- Binary breakthrough example 46

Figure 15- Dead volume and dead time system scheme. 46

Figure 16- CO_2 breakthrough curve for dead volume calculation 47

Figure 17- Fixed bed scheme 50

Figure 18- N_2 adsorption/desorption isotherm on zeolite 13X at -196 °C. 63

Figure 19- Pure CO_2 and N_2 experimental adsorption isotherms at 50 °C on zeolite 13X. 64

Figure 20- CO_2 (black) and N_2 (red) pure adsorption isotherms at 25 °C (circle), 50 °C (square) and 75 °C (triangle) on zeolite 13X. Symbols for experimental data and dashed line represents Sips model fitting. 65

Figure 21- CO_2 (black) and N_2 (red) pure adsorption isotherms at 25 °C (circle), 50 °C (square) and 75 °C (triangle) on zeolite 13X. Symbols for experimental data and solid line represents Toth model fitting. 66

Figure 22- Binary adsorption isotherm for CO_2-N_2 (15/85 % in molar basis) at 50 °C on zeolite 13X. Symbols represent experimental data and solid line represents Extended Sips model fitting..... 68
Figure 23- Repeatability test: CO_2 (15 % v/v) breakthrough at 50 °C..... 69
Figure 24- Comparison between static and dynamic tests for reproducibility. Black symbols represent isotherm experimental data; red symbols represent fixed bed adsorption capacity from breakthroughs. 70
Figure 25- Experimental breakthrough curve for CO_2-N_2 (15/75 % v/v) in He (10 % v/v) at 25, 50 and 75 °C on zeolite 13X..... 71
Figure 26- CO_2 (black) and N_2 (red) pure adsorption isotherms at 25 °C (circle), 50 °C (square) and 75 °C (triangle) on zeolite 13X. Symbols are experimental data and round dots represent DSL model fitting. 72
Figure 27- Breakthrough curve for CO_2 -N_2 (15/75 % v/v) in He (10 % v/v) at 25 °C. 1bar. Symbols represent experimental data; lines and dashed lines represent simulated data. 73
Figure 28- Breakthrough curve for CO_2 -N_2 (15/75 % v/v) in He (10 % v/v) at 50 °C. 1bar. Symbols represent experimental data; lines and dashed lines represent simulated data. 74
Figure 29- Breakthrough curve for CO_2 -N_2 (15/75 % v/v) in He (10 % v/v) at 75 °C. 1bar. Symbols represent experimental data; lines and dashed lines represent simulated data. 74
Figure 30- Mass transport coefficient (K_{LDF}) sensibility for breakthrough experiments. 76
Figure 31- (a)Adiabatic and non-adiabatic breakthrough curve for CO_2-N_2 (15/75 % v/v) in He (10 % v/v) at 50 °C. (b) Gas temperature (Tg) and wall temperature (Tw) profile at the column exit for adiabatic and non-adiabatic conditions. 77
Figure 32- Adsorption-desorption (*configuration 1*) process for CO_2-N_2 separation. 80
Figure 33- Time for adsorption and *configuration 1* regeneration strategy. 82
Figure 34- Adsorption- desorption (*configuration 2)* process for CO_2-N_2 separation. 83
Figure 35- Time for adsorption and *configuration 2* regeneration strategy. 84
Figure 36- Pure CO_2 desorption isotherm at 50 °C (black) and at 150 °C (red) on zeolite 13X. Symbols represent experimental data; solid line represents DSL model fitting..... 88

Figure 37- Adsorption- desorption (*configuration 2*) process for CO_2-N_2 separation. Symbols represent experimental data and solid line represents simulated data. 89
Figure 38- Adsorption- desorption (*configuration 2*) process for CO_2-N_2 separation with different purge flowrate. Symbols represent experimental data and solid line represent simulated data..... 90

LIST OF TABLES

Table 1 - Non-linear isotherm model equations. 22
Table 2 - Dead volume for FBU 47
Table 3 - Particle and bed parameters. 59
Table 4 - Mass transfer parameters. 60
Table 5 - Energy transfer parameters 61
Table 6 - Momentum parameters. 62
Table 7 - Textural properties of the adsorbent 64
Table 8 - Fitting parameters of Sips and Toth models for pure adsorption isotherms of CO_2 and N_2 on zeolite 13X in the temperature range 25–75 °C for 0–10 bar. 67
Table 9 - Average Relative Error (ARE) for Sips and Toth model on adsorption experimental data fitting. 68
Table 10- Fitting parameters of Extended Sips model for CO_2 and N_2 (15/85 % v/v) binary isotherm at 50 °C 69
Table 11- Fixed bed adsorption capacity for CO_2. 71
Table 12- Fitting parameters of DSL model for pure adsorption isotherms of CO_2 and N_2 on zeolite 13X in the temperature range 25–75 °C for 0–10 bar. 73
Table 13- Comparison between fixed bed adsorption capacity and amount adsorbed for CO_2 in Toth and DSL isotherm model. 75
Table 14- Physical Properties of the adsorbent 78
Table 15- Physical Properties of the fixed bed. 79
Table 16- Some model parameters temperature dependence between 25 and 300 °C. 79
Table 17- CO_2 recovery by *configuration 1* 81
Table 18- CO_2 recovery by *configuration 2* 84
Table 19- Energy to heat He purge and He purge volume per mole of CO_2 desorbed in *configuration 2* 85
Table 20- Readjusted K_{LDF} values for CO_2 at desorption for different purge flowrates. 91

NOMENCLATURE

$(-\Delta H)$	Heat of adsorption
$\Delta t_0+\Delta t_1$	Dead time
b	Equilibrium constant
B_o	Buoyancy effect
C	Total concentration
C_g	Gas mixture concentration
$C_{g,i}$	Gas concentration of component i
C_i	Outlet concentration of component i
C_{io}	Inlet concentration of component i
C_{pg}	Gas calorific capacity at constant pressure
$C_{pg,i}$	Gas calorific capacity at constant pressure of component *i*
C_{ps}	Solid calorific capacity at constant pressure
C_{pw}	Wall calorific capacity at constant pressure
C_{vg}	Gas calorific capacity at constant volume
D_{ax}	Axial mass dispersion coefficient
$D_{ax,i}$	Axial mass dispersion coefficient of component *i*
$D_{e,i}$	Effective diffusivity of component *i*
d_{ext}	External column diameter
d_i	Column internal diameter
D_{ij}	Binary diffusivity
$D_{m,i}$	Molecular diffusivity of component *i* in the mixture
d_p	Particle diameter
E	Total energy per volume unit
E_{He}	Energy required to heat the He purge per mole of CO2 desorbed
E_k	Kinetic energy
E_p	Potential energy
F_e	Energy flux
F_m	Mass flux
h_w	Heat transfer coefficient between the gas and the wall
IP_{ji}	DSL Isotherm model parameter *j* of component *i*
k	Henry's Law constant
K_g	Gas conductivity
$K_{g,i}$	Gas conductivity of component *i*
K_{LDF}	Linear Driving Force (LDF) mass transfer coefficient
K_w	Wall conductivity
L	Avogadro number
L_o	Bed length

m_{ads}	Adsorbent mass
m_{exc}	Excess mass
M_i	Molar mass of component *i*
n	Heterogenity parameter
n_{ads}	Number of moles adsorbed
n_f	Number of moles in fluid phase
n_{He}	Number of moles of He purge
n_m	Specific monolayer capacity
NoC	Number of components
n_r	Number of moles retained
Nu	Nusselt number
P	Pressure
P_{atm}	Atmospheric pressure
P_i	Partial pressure of component *i*
P_o	Saturation pressure
Pr	Prandtl number
Q	Volumetric flowrate
$q_{e,i}$	Adsorption equilibrium concentration of component *i*
q_{eq}	Adsorbed concentration of component i in equilibrium
q_i	Average adsorbed concentration of component i
q_{max}	Adsorbed concentration at complete coverage
R^2	Linear correlation coefficient
Re	Reynolds number
R_g	Ideal gas constant
r_p	Particle radius
S_{BET}	BET specific surface area
T	Temperature
T_{ads}	System temperature at adsorption experiments
T_{ads}	Adsorption temperature
T_{air}	External air temperature
t_b	Breakthrough time
t_e	Saturation time
T_g	Gas temperature
T_{reg}	Regeneration temperature
T_s	Solid temperature
t_{st}	Stoichiometric time
T_w	Wall temperature
u	Intersticial velocity

U	Internal energy
U_o	Overall heat transfer coefficient between the column wall and the external air
v	Superficial velocity
V_b	Volume of the components in the balance
V_{col}	Volume of the column
V_d	Dead Volume
V_{He}	Amount of He purge volume per mole of CO2 desorbed
v^{inlet}	Inlet superficial velocity
V_{mp}	Specific micropore volume
V_p	Specific pore volume
V_s	Specific solid volume
y_i	Molar fraction of component *i*
α_w	Ratio of the internal surface area to the volume of the column wall
α_{wl}	Ratio of the logarithmic mean surface area of the column shell to the volume of the column
λ_e	Heat axial dispersion coefficient
μ_g	Gas viscosity
ρ_b	Bed density
ρ_g	Gas density
ρ_w	Wall density
σ	Adsorptive molecular sectional area
ε	Bed porosity
ε_p	Particle porosity

SUMMARY

1 INTRODUCTION 16
1.2 Objective 18
2 LITERATURE REVIEW 19
2.1 Theory of Gas Adsorption 19
2.2 Gas Physisorption Isotherms 19
2.3 Equilibrium Isotherm Modeling 20
2.3.1 Linear Isotherm 21
2.3.2 Non-linear Isotherms 21
2.4 Carbon Dioxide (CO_2) Separation by Adsorption 23
2.4.1 Adsorbents for CO_2 capture ***25***
2.5 Breakthrough Experiments 27
2.6 Regeneration of Adsorbents in Adsorption-Desorption Cycles 30
3 EXPERIMENTAL 34
3.1 Materials 34
3.2 Methodology 34
3.2.1 Adsorbent Textural Properties ***34***
3.2.2 Gas Isotherms 37
3.2.3 Breakthrough and Desorption Experiments 39
3.2.4 Breakthrough and Desorption simulations 48
4 MATHEMATICAL MODEL FORMULATION 49
4.1 Mass Balance 49
4.2 Energy Balance 54
4.3 Momentum Balance. 58
4.4 Parameters determination 58
4.4.1 Particle and bed parameters 59
4.4.2 Mass transfer parameters 59
4.4.3 Energy transfer parameters 60
4.4.4 Momentum Parameters 61
4.5 Numerical method and software 62
5 RESULTS AND DISCUSSION 63
5.1 Adsorbent textural properties 63
5.2 Gas pure and binary isotherms for CO_2 and N_2 64
5.3 Breakthrough experiments and simulations 69

5.4 Desorption experiments and simulations..... 80
6 CONCLUSION 92
6.1 Suggestions for future work..... 93
REFERENCES 94

1. INTRODUCTION

1.1. Relevance and contextualization

Even though there is no worldwide consensus on the origin, there is growing support for the claim that global climate change is happening, and many climate scientists consider that a major cause is the anthropogenic emission of greenhouse gases (GHGs) into the atmosphere [1]. Fossil fuels combustion produces GHGs, and certainly the use of them for energy contributes to a number of environmental problems globally [2]. Unfortunately, fossil fuels are the dominant source of the global primary energy demand, and will likely remain so for the next several decades. Carbon dioxide (CO_2), as a primary greenhouse gas, is regarded as one of the main promoters for climate change [3]. Therefore, any approach on behalf of decreasing CO_2 emissions is transcendent.

Different approaches may be adopted to reduce CO_2 emissions: i) improving energy efficiency, ii) increasing usage of low carbon fuels (e.g., natural gas, hydrogen or nuclear power), iii) expanding usage of renewable energy (e.g., solar, wind, hydropower and bioenergy), iv) applying geoengineering approaches (e.g. afforestation and reforestation) and v) CO_2 capture and storage (CCS) [4]. CCS may be regarded as a transitional bet for CO_2 emission reduction until accomplishing overall extensive use of 100% clean energy sources. CCS consists of the separation of CO_2 from industrial and energy-related sources, transport to a storage location and long-term isolation from the atmosphere. However, the widespread application of CCS would depend on technical maturity, costs, diffusion and transfer of the technology to developing countries [5]. CO_2 separation is considered the most expensive step (60-70% of total cost) in the CCS chain and thereupon its significance [6]. Currently, there are mainly three technological paths that can be pursued for CO_2 capture from gas or coal-derived power generation [1]: post-combustion capture, pre-combustion capture and oxy-fuel combustion capture.

Post-combustion capture consists of removal of CO_2 from flue gas arising from the thermal power plant combustion chamber [7]. In pre-combustion capture, primary fuel is reacted to yield syngas (mainly CO and H_2). The syngas is later passed through a catalytic reactor to give CO_2 and more H_2. The CO_2 is then separated and the H_2 is used as fuel in a gas turbine combined-cycle plant [2, 8]. Oxy-fuel combustion is actually modified post-combustion method. Fuel reacts with almost pure oxygen in place of air, which results in a high concentration of CO_2 in flue gases

[2]. Most of research interest sticks to post-combustion capture since it can be more easily retrofitted to existing power plants once radical changes in the plants are not necessary [9].

In order to achieve CO_2 separation in any of the previous scenarios, several processes are available and these include absorption, adsorption, membrane and cryogenics [2, 7]. The selection of a suitable separation method is crucial and relies on the characteristics of the flue gas stream, which depends principally on the power-plant technology [2].

Although absorption is currently the leading and most mature CO_2 separation technique in post-combustion scenario, research on CO_2 capture by adsorption is continuously growing to be a feasible economic alternative once it is a dry method, so that no by-product such as wastewater is formed as in conventional absorption process [7]. Adsorption requires the use of a solid (adsorbent material) packed in a column, generally forming a fixed bed (may be a fluidized bed as well), in which a gas mixture component is preferentially adsorbed to the material surface. Nevertheless, the practical applicability of this methodology hinges essentially on the selection of the adsorbent and the regeneration strategy [10].

An ideal theoretical adsorbent might exhibits, but not exclusively, features like fast adsorption and desorption kinetics, huge adsorption capacity and infinite regenerability and stability. However, actual adsorbents have trade-offs and as a result their effectiveness must be evaluated in the context of a complete CO_2 adsorption-desorption separation process [11]. Despite efforts on development of modified adsorbents with enhanced CO_2 adsorption capacity [12-18], commercial adsorbents are still favorite for industrial purposes once they can be produced in large scale and not only for laboratorial testing issues.

With regard to the regeneration strategy, the recovery of the adsorbed components is traditionally executed by either decreasing system pressure (Pressure Swing Adsorption, PSA) or increasing system temperature (Temperature Swing Adsorption, or TSA). PSA is conventionally used for bulk separations and TSA for purification issues [19]. Even though PSA would fit better into CO_2 capture in post-combustion scenario, TSA interest has grown recently once the desorption configuration is likely to be optimized to minimize the total cycle time. Another reason is the possibility of energy integration in the power plants that could reduce the cost of heating and make the process economically feasible.

The whole TSA process basically comprises two steps: adsorption and desorption (also known as regeneration). In the course of adsorption, the gas mixture is continuously fed to the

column and the system temperature is kept constant whereas during desorption, the gas stream feeding is stopped and temperature is immediately swing to higher values to recuperate the adsorbed molecules. In large-scale industrial plants, TSA is actually performed employing at least two fixed beds, one performing adsorption while the other is being regenerated. The adsorption process has been extensively covered in the literature, while the desorption step has gained less attention and, hence, has yet to be studied more deeply. The desorption study relevance is even more meaningful for separation process via TSA than in PSA since it is easier to integrate adsorption-desorption stages in the latter once pressurization and depressurization are usually a matter of seconds. On the contrary, the time synchronization for adsorption-desorption process by TSA is more complex since thermal equilibrium is not instantaneous and many parameters are affected by the gradual rise in temperature during heating.

1.2. Objective

This work primary purpose is assessing TSA configurations by means of developing adsorption-desorption experiments and simulations in a single fixed bed unit for CO_2 separation within post-combustion scenario from a desulfurized dry flue gas stream (CO_2-N_2, 15/85 % v/v) using commercial adsorbent binderless zeolite 13X. Desorption via TSA and inert gas purge is assessed altogether and separately with the aim of establishing an optimum regeneration outline for an efficient recovery of the adsorbed product.

Simulation of the whole adsorption-desorption process is performed in order to provide a breakthrough and desorption model that could predict the system behavior when modifying input parameters. Numerical resolution of the mathematical model proposed is carried out employing gPROMS software. Model is validated with experimental data of both adsorption and desorption experiments.

2. LITERATURE REVIEW

2.1. Theory of Gas Adsorption

Adsorption occurs whenever a solid surface is exposed to a fluid: it is defined as the enrichment of material or increase in the density of the fluid in the vicinity of an interface [20, 21]. Per definition, the solid is called the adsorbent and the gas, in the fluid phase, is called the adsorptive. The fluid in the adsorbed state is called adsorbate [22].

Adsorption can be physical (physisorption) or chemical (chemisorption). Physisorption is a general phenomenon occurring whenever an adsorptive is carried into contact with the surface of a solid (the adsorbent). The intermolecular forces involved are of the same type as those responsible for the imperfection of real gases and the condensation of vapors. In addition to the attractive dispersion forces and the short-range repulsive forces, specific molecular interactions (e.g., polarization, field-dipole, field gradient quadrupole) generally occur because of particular geometric and electronic properties of the adsorbent and adsorptive. In chemisorption, the intermolecular forces involved lead to the formation of chemical bonds [21].

2.2. Gas Physisorption Isotherms

The amount of gas adsorbed, n_{ads}, by the mass, m_{ads}, of solid (adsorbent) is a function of the equilibrium pressure, P, the temperature, T, and the nature of the gas–solid system. For a given gas adsorbed on a particular solid at a constant temperature, we may write:

$$\frac{n_{ads}}{m_{ads}} = f(P)T \tag{1}$$

Moreover, if the gas is below its critical temperature, it is possible to write:

$$\frac{n_{ads}}{m_{ads}} = f(P/P_o)T \tag{2}$$

Where P_o is the saturation pressure of the adsorptive at temperature T.

Equations (1) and (2) represent the adsorption isotherm which is the relationship between the amount adsorbed by unit mass of solid and the equilibrium pressure (or relative pressure), at a known temperature [20]. In order to facilitate the comparison of adsorption data, it is highly suggested that adsorption isotherms are presented in graphical form with the amount adsorbed (preferably in $mol \cdot g^{-1}$) plotted against the equilibrium relative pressure (P/P_o), or against P, when the temperature is above the critical temperature of the adsorptive. If the adsorption measurements are made under conditions where the gas phase deviates significantly from ideality (e.g., at high pressure), it is preferable to present the isotherms in terms of gas fugacity rather than pressure [21].

The IUPAC published in 1985 a classification of six sorption isotherms based upon an extensive literature survey performed by Bruneuer, Demming, Demming and Teller (BDDT) [22]. However, over the past 30 years various new characteristic types of isotherms have been identified and shown to be closely related to particular pore structures. The proposed updated classification of physisorption isotherms, which are detailed described elsewhere [21] is shown in Figure 1.

Figure 1.Classification of physisorption isotherms

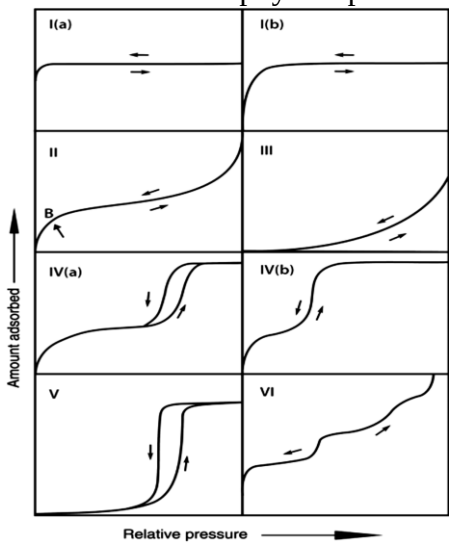

Source: [21]

2.3. Equilibrium Isotherm Modeling

Innumerable isotherm equations have been employed to describe the equilibrium characteristics of adsorption. Both the sorption mechanism and the surface properties and affinity

of the sorbent can be understood from the equation parameters and the underlying thermodynamic assumptions of these isotherm models [23]. Accuracy of an isotherm model is normally dependent on the number of independent parameters in the model, whereas its popularity in relation to process application is usually a function of its mathematical simplicity [24].

2.3.1. Linear Isotherm

The linear isotherm model (Henry's law), for instance, has only two independent parameters, and consequently is applicable to only a limited class of adsorption systems [24].

$$q_e = kP \tag{3}$$

where q_e is the amount of adsorbate in the adsorbent at equilibrium, P is the pressure at equilibrium and k represents the Henry's law constant.

Henry's law is mainly applicable to low coverage. This model is generally used as reference to check thermodynamics consistency of non-linear isotherms since they should reduce to linear behavior when loading tends to zero (i.e., as $P \rightarrow 0$, $(dq_e/dP)_T \rightarrow constant$) [24, 25].

2.3.2. Non-linear Isotherms

Isotherm model formulation can generally be classified in terms of three fundamental approaches: *i)* kinetic considerations, *ii)* thermodynamics and *iii)* third approach which is based on the potential theory. The main idea behind this theory is the generation of the characteristic curve. The minimum number of parameters required to fit a nonlinear isotherm is three, as in the elementary Langmuir isotherm model [24].

Langmuir adsorption isotherm was originally developed to describe gas–solid-phase adsorption onto activated carbon. This classic empirical model was conceived in its formulation assuming monolayer adsorption (i.e., the adsorbed layer is one molecule in thickness), with adsorption phenomenon only occurring at a determinate (fixed) number of definite localized sites, that are identical and equivalent, with no lateral interaction and steric hindrance between the

adsorbed molecules, even on neighboring sites. Langmuir isotherm refers to homogeneous adsorption, where each molecule owns constant enthalpies and sorption activation energy (all sites possess equal affinity for the adsorbate), with no transmigration of the adsorbate in the plane of the surface. Graphically, it is characterized by a plateau, an equilibrium saturation point where once a molecule occupies a site, no further adsorption can take place [26]. The mathematical expressions of Langmuir isotherm and other non-linear models are specified in Table 1.

Table 1. Non-linear isotherm model equations.

Isotherm	Non-linear form	Direct multicomponent extension	NIP*	$\left(\frac{\partial q_e}{\partial P}\right)_T$ $as\ P \to 0$	Reference
Langmuir	$\frac{q_e}{q_{max}} = \frac{bP}{1+bP}$	$\left(\frac{q_e}{q_{max}}\right)_i = \frac{b_i P_i}{1+\sum_{j=1}^{NoC} b_j P_j}$ *j=1,2,…,N.*	3	Constant	[27]
Freundlich	$q_e = bP^{1/n}$	Not applicable	3	Varying	[28]
Sips	$\frac{q_e}{q_{max}} = \frac{(bP)^{1/n}}{1+(bP)^{1/n}}$	$\left(\frac{q_e}{q_{max}}\right)_i = \frac{(b_i P_i)^{1/n_i}}{1+\sum_{j=1}^{NoC}(b_j P_j)^{1/n_j}}$ *j=1,2,…,NoC.*	4	Varying	[29]
Toth	$\frac{q_e}{q_{max}} = \frac{bP}{[1+(bP)^n]^{1/n}}$	Not applicable	4	constant	[30]

*Number of independent Parameters (NIP)

Source: own authorship.

Parameter q_{max} represents the amount adsorbed per mass of adsorbent corresponding to the complete coverage; *1/n* is a measure of the surface heterogeneity, ranging between 0 and 1, becoming more heterogeneous as its value gets closer to zero [31] and *b* denotes an equilibrium constant.

Freundlich isotherm is the earliest known model describing the non-ideal and reversible adsorption, not restricted to the formation of monolayer [26]. The Freundlich equation, unlike the Langmuir one, does not become linear at low concentrations nor does it exhibit a saturation value but remains convex to the concentration axis. The shape of the isotherm is such that *1/n* is a number below unity. There is no guarantee that Freundlich equation derivation is unique; subsequently, if the data fit the equation, it is only likely, but not ascertained, that the surface is heterogeneous [32].

Sips isotherm is a combination of the Langmuir and Freundlich isotherm type models and is likely to describe heterogeneous surfaces much better. At low adsorbate concentrations, it reduces to a Freundlich isotherm; however at high adsorbate concentration, it predicts a monolayer adsorption capacity representative of the Langmuir isotherm and hence and does not follow Henry's law [26, 33, 34]. Toth isotherm model is another empirical equation developed to improve Langmuir isotherm fittings, and is advantageous in describing heterogeneous adsorption systems, which fulfills both low and high-end boundary of the concentration [26].

2.4. Carbon Dioxide (CO_2) Separation by Adsorption

Adsorptive separation (Figure 2) is a mixture separating process which works on the principle of differences in adsorption/desorption properties of the mixture components [3]. The adsorbed CO_2 can be recovered either by reducing pressure (Pressure-Swing Adsorption or PSA), or by increasing temperature (Temperature Swing Adsorption, or TSA) or by passing an electric current through the adsorbent (Electrical Swing Adsorption, or ESA) or process hybrids (PTSA) or washing [2].

Some limitations make this process less effective such as [7]:

- Low selectivity and capacity of available adsorbent for CO_2.
- Lower removal efficiency as compared to other technologies such as absorption and cryogenic.
- Regeneration and reusability of adsorbent.

Figure 2. Schematics of adsorption, carbon capture process in a cylindrical bed.

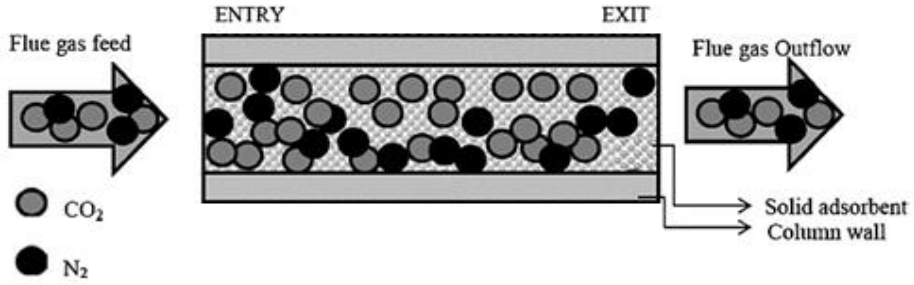

Source: Modified from [3].

Songolzadeh *et al.* (2012) , in their review on adsorbents for CO_2 capture and storage, indicated that CO_2 adsorbent must have high selectivity and adsorption capacity, adequate adsorption/desorption kinetics, remain stable after several adsorption/desorption cycles, and possess good thermal and mechanical stability.

The adsorbents may have pores in the form of slits, cylinders or cages interconnected by pore windows. When pore sizes or pore windows are of molecular size, they can separate gas molecules by equilibrium, kinetic or molecular sieving mechanisms as observed in Figure 3 [36].

Figure 3. Types of separation by adsorption: A) equilibrium, (B) kinetic, or (C) molecular sieving mechanisms. Large balls represent N_2 molecules and small ones CO_2.

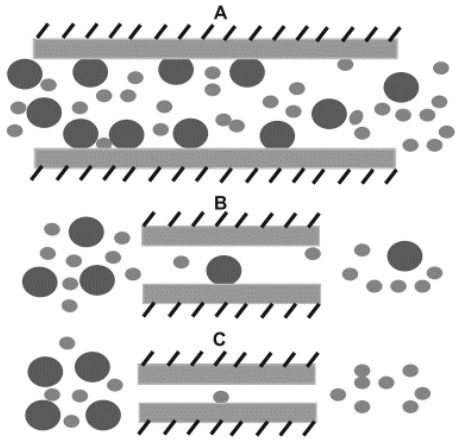

Source: [36]

The gas molecules have different effective kinetic diameters within the solids and gases. CO_2 appears to have a smaller kinetic diameter than N_2 in microporous solids. In the gas phase, CO_2 has a larger kinetic diameter than N_2. The exact values appear to be substrate dependent, but values of 3.3 and 3.8 Å were suggested for CO_2 and N_2 in zeolites, respectively. When the pore windows are much larger than the dimensions of CO_2 and N_2, the potential for the separation of CO_2 and N_2 is determined by the differential equilibrium distribution of these molecules, as shown in Figure 3A. When the opening of the pore apertures is a little larger than the size of the N_2, the selectivity of CO_2 over N_2 of the adsorbent is enlarged by the difference between the diffusivities. The diffusivity of N_2 is considerably reduced when the pore window aperture dimensions approximate 3.8 Å; in contrast, CO_2 diffusivity still fits well with the pore window (Figure 3B). If

the pore window is smaller than 3.8 Å, the CO_2 and N_2 mixture can be sieved molecularly (Figure 3C) [36].

2.4.1. Adsorbents for CO_2 capture

Adsorbents, which could be applied to CO_2 capture, include activated carbons, carbon fibers, silica gel, ion-exchange resins, zeolites, and porous silicates (SBA-15, MCM-41, etc.), activated alumina, metal oxides (CaO, MgO, K_2O, Li_2O), metal-organic frameworks (MOFs), organic–inorganic hybrid sorbents and other surface-modified porous media [35].

The adsorbents used for CO_2 capture can be classified into two categories: physical and chemical adsorbents.

2.4.1.1. Physisorbents

Physisorbents are those who undergo relatively weak interactions with the adsorbate in the interface gas-solid. Microporous physisorbents have interconnected pores with molecule-sized pore windows, and can be used to separate gas molecules via equilibrium, kinetic, or molecular sieving mechanisms. These adsorbents can be crystalline or amorphous. Crystalline adsorbents have remarkably narrow pore-size distributions, due to their well-defined atomic positions, whereas amorphous adsorbents have broader pore-size distributions, due to the more random distribution of bond angles and bond lengths among their atoms. Zeolites and metal organic frameworks (MOFs) are crystalline microporous adsorbents, while carbon molecular sieves (CMS) and microporous polymers are amorphous microporous adsorbents. Both classes are currently being studied broadly for their properties as CO_2 adsorbents, and for their potential use as CO_2 sorbents in adsorption-based gas separation [36].

2.4.1.2. Zeolites

Zeolites are porous crystalline structure materials containing pores of molecular size (5-12 A˚ or 0.5-1.2 nm). The term zeolite is derived from the Greek words for "boiling stone" from

the ability of these materials to adsorb water and release it by heating. Conventional zeolites are based on silicate structures in which the substitution of some of the Si by Al (or other metals) leads to a negative charge on the structure, with cations (usually Na or other alkali or alkaline earth metals) within the structure of pores. This leads to another important property, the ion exchange, in which the metal ions in the pore structure can be replaced by other cations (e.g., metal, ammonium, quaternary ammonium). The zeolite structures are networks made up of tetrahedral T atoms (T = Si, Al, etc.) bound by oxygen ions forming an open crystalline circuit that has pores of molecular sizes [37]. Since the micropore structure is determined by the crystal lattice, it is uniform with no pore size distribution. This characteristic is what differentiates zeolites from other microporous adsorbents [38].

Zeolites occur naturally and are generally formed in alkaline environments of sediments and volcanic materials. Many of these materials have valuable properties as adsorbents and even catalysts, but the natural forms often have flaws and irregularities in their structures that limit their application. The development of laboratory methods for synthesizing zeolites was fundamental to lead to many commercial applications of zeolites. Linde Laboratories (Tonawanda, New York) pioneered zeolite syntheses [37]. The application of zeolites in the gas separation context is focused predominantly on the upgrading of natural gas and CO_2 capture in post-combustion scenario. According to the International Zeolite Association (IZA), there are currently more than 170 unique molecular topologies known, which introduces the possibility of studying the effect of composition, or certain structural or chemical characteristics on the adsorption separation effectiveness given the enormous diversity of zeolite materials (Figure 4) [39].

Figure 4. Diversity of zeolite structures

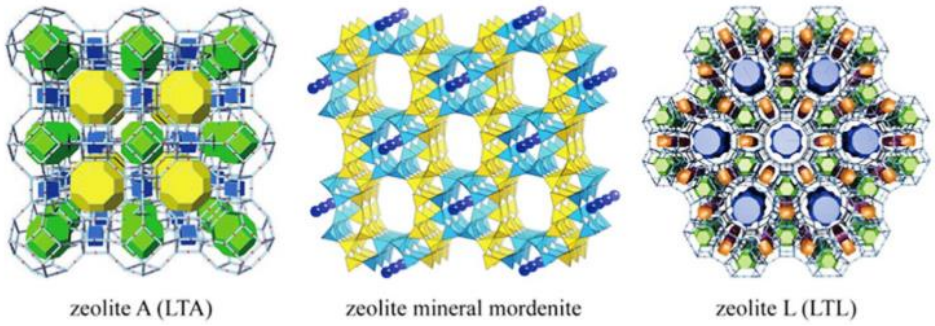

Source: [39]

In general, zeolites have shown encouraging results for separation of CO_2 from gas streams. CO_2 separation via zeolites is favored by the relatively large energetic dipole and quadruple of CO_2, which strongly interacts with the electric field created by the structural cations of zeolites [40].

Among the different kind of zeolites, zeolite 13 X has been suggested as a promising adsorbent for CO_2 separation from N_2 due to its high adsorption capacity as reported by Harlick & Handan Tenzen (2004) in their experimental adsorbent screening study of 13 zeolite based adsorbents. Similarly, zeolite 13 X stands out when compared to other type of materials as described by Bahamon & Veja (2016) in their systematic evaluation of materials for CO_2 adsorption in a post-combustion scenario using TSA technique. They assessed 11 different adsorbents by means of simulations of *Grand Canonical Montecarlo* and concluded that Mg-MOF-74 is the most promising material to be used in such TSA processes; however, considering its current availability on a large scale and from the economic point of view, zeolite 13X still remains today as a preferred candidate for industrial processes. All of the above justifies the use of this material to evaluate its performance in TSA configurations experimentally and by simulations.

2.4.1.2. Chemisorbents

Chemisorbents display properties that give them the potential to be applied for the separation of CO_2 from flue gases, and as sorbents for the chemical looping cycle (CLC). Current research focuses on weak chemisorbents such as amine supported materials, and strong chemisorbents such as strong bases [36].

Strong chemisorbents include materials like alkaline metal oxides (Na_2O, K_2O) and alkaline earth metal oxides (CaO, MgO), on which the CO_2 molecules can adsorb forming mono- or multidentate species [11].

2.5. Breakthrough Experiments

Breakthrough curves are elementary but important operations since they can be used to determine the adsorption equilibrium, to extract the mass transfer and heat transfer kinetics and also to examine the characteristics of the column [43].

The S-shaped curve in Figure 5 represents monocomponent breakthrough behavior in a fixed bed, where eluent concentration (or normalized eluent concentration) is plotted against time.

Figure 5. Monocomponent Breakthrough Curve.

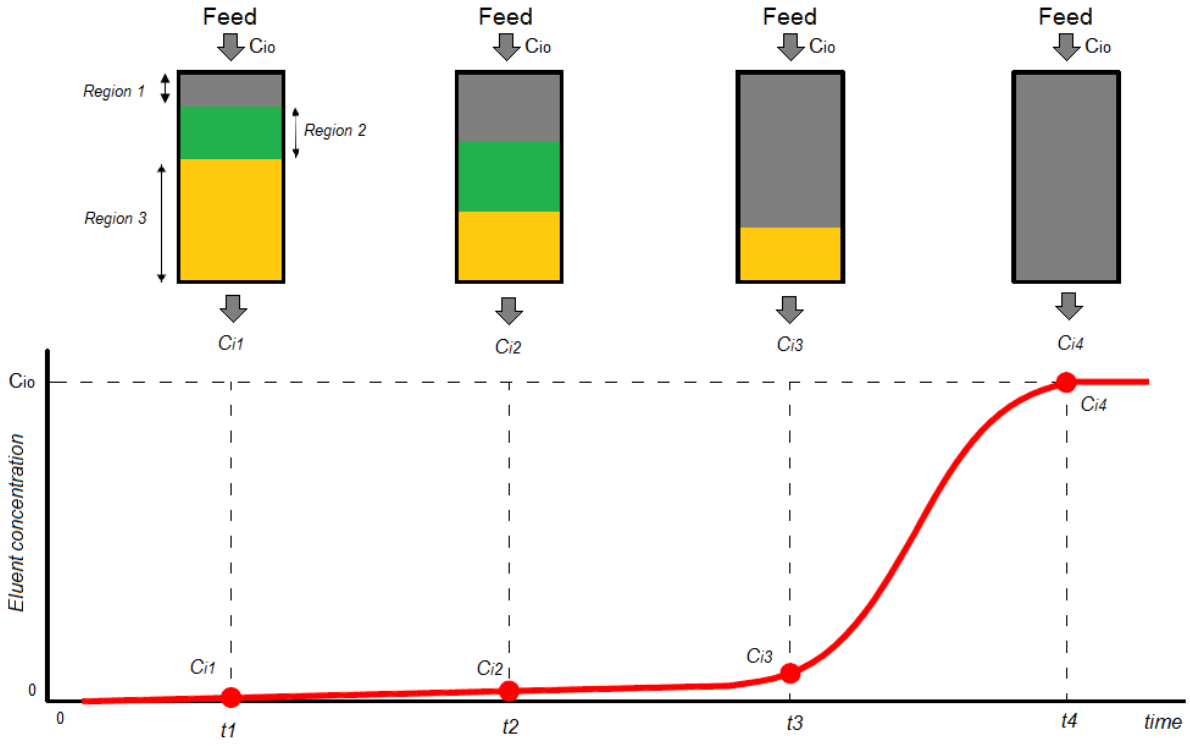

Source: own authorship.

The resultant concentration profile can be better explained by observing the relation between the four times (t_1, t_2, t_3, t_4) and the four eluent concentrations (C_{i1}, C_{i2}, C_{i3}, C_{i4}). At t_1, the column has three differentiated regions: region 1 (grey) which symbolizes the saturated length of the bed, region 2 (green) which represents the Mass Transfer Zone (MTZ), where adsorption is occurring, and the region 3 (yellow) that embodies the length of unused bed (LUB). At t_2, the MTZ advances as saturation length of the bed increases. At t_3, the leading point of MTZ has reached the end of the bed and the concentration of the eluent C_i is no longer zero; this moment is usually denoted as breakthrough point (t_b). The breakthrough concentration $C_{i,b}$ (C_{i3} in Figure 5) can be assumed as the minimum detectable or maximum allowable solute concentration in the eluent fluid [44], often referred as to an arbitrary value between 0.01 to 0.05 of C_{i0}. Finally, at t_4, the bed has reached total saturation. Thus, eluent concentration (C_{i4}) equals initial solute concentration C_{i0}.

The stoichiometric time (t_{st}), which splits the MTZ into equal areas A and B as shown in Figure 7 and corresponds to the ideal wave-front velocity (green line) [44], is a key parameter for breakthrough experiments as will be further discussed in the methodology section. The grey area in Figure 6 denotes the actual fraction of bed capacity.

Figure 6. Breakthrough curve (normalized eluent concentration, C_i/C_{io} vs time).

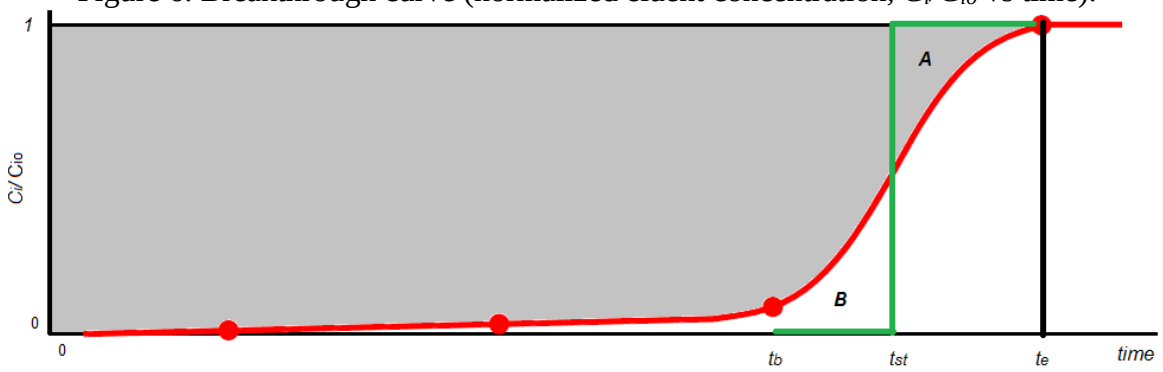

Source: own authorship.

For binary breakthrough experiments in a fixed bed, a common phenomenon is the overshoot pattern in the eluent concentration of some components exceeding their inlet value [43]. The overshoot behavior of N_2, as illustrated in Figure 7, can be explained by the displacement of the weaker component N_2 to the end of the column after being pushed by the propagation of the CO_2 front in the packed bed. Therefore, the outlet N_2 concentration will be higher than the inlet one, hence causing the roll-up effect [45]. Then, when strongly adsorbed component begins to exit the fixed bed, the weaker component starts to return to its inlet concentration.

Figure 7. Multicomponent Breakthrough Curve.

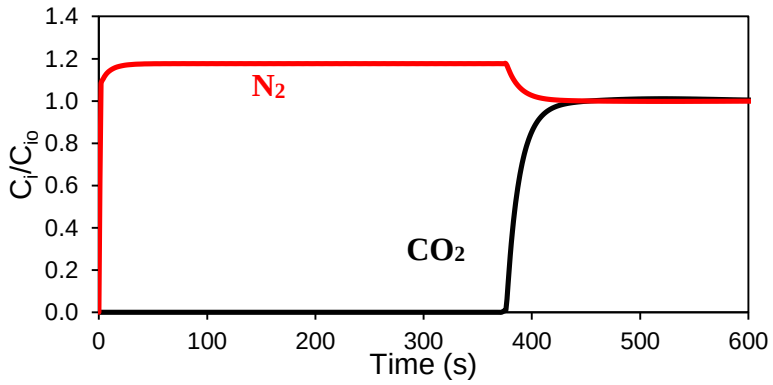

Source: own authorship

2.6. Regeneration of Adsorbents in Adsorption-Desorption Cycles

Processes based on adsorption are predominantly of two kinds according to the way in which the adsorbate is changed between the adsorption and desorption steps: by fluctuating the pressure or the temperature [46].

In pressure-swing adsorption (PSA), adsorption takes place at an elevated pressure, whereas desorption occurs at near-ambient pressure, as shown in Figure 8.

Figure 8. Schematic representation of PSA and TSA.

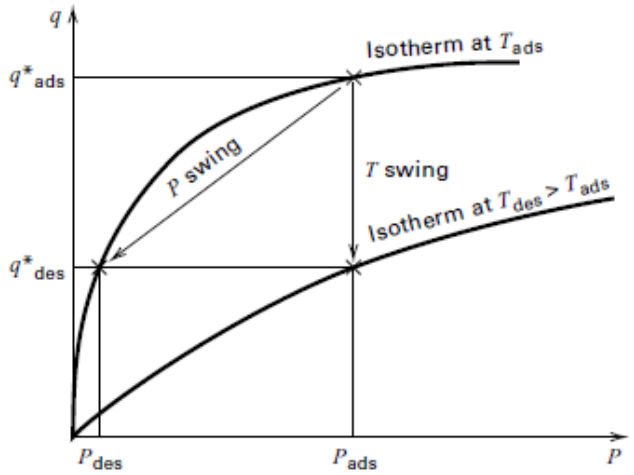

Source: [44].

PSA is employed for bulk separations because the bed can be depressurized and repressurized rapidly, making it possible to operate at cycle times of seconds to minutes. Because of these short times, the beds do not need to be large even when a substantial fraction of the feed gas is adsorbed. If adsorption takes place at near-ambient pressure and desorption under vacuum, the cycle is referred to as vacuum-swing adsorption (VSA). PSA and VSA are widely used for air separation [44].

In thermal (temperature)-swing-adsorption (TSA), the adsorbent is regenerated by desorption at a temperature higher than used during adsorption, as shown in Figure 8. Bed temperature is increased by (1) heat transfer from heating coils located in the bed, followed by pulling a moderate vacuum or (2) more commonly, by heat transfer from an inert, nonadsorbing, hot purge gas, such as steam. Following desorption, the bed is cooled before adsorption is resumed. Because heating and cooling of the bed requires hours, a typical cycle time for TSA is hours to

days. The desorption temperature is high, but not so high as to cause deterioration of the adsorbent. TSA is best applied to removal of contaminants present at low concentrations in the feed so that nearly isothermal adsorption and desorption is achieved. The heating and cooling steps cannot be accomplished instantaneously because of the low bed thermal conductivity. Although heat transfer can be done indirectly from jackets surrounding the beds or from coils within the beds, temperature changes are more readily achieved by preheating or precooling a purge fluid [44].

In order to diminish cycle time and low CO_2 purity during regeneration when Temperature swing is performed by hot purge gas, Clausse *et al* (2011) had the idea of applying indirect heating during the regeneration step using an internal heat exchanger. Heating was applied in a two-phase heat transfer method, specifically steam condensation, while a small purge can be used to help to increase the desorption rate by pushing out the desorbed component and by lowering its partial pressure. This allows reaching high heat transfer coefficients, which reduces the regeneration time. During the adsorption step, the adsorber is cooled by water circulation that allows removing the adsorption heat and limits the impact of the inlet gas temperature. Then, the adsorbent capacity is kept maximal.

Ntiamoah *et al.* (2016) used the CO_2 product itself as the regeneration purge gas in fixed bed TSA systems. This guaranteed them to maintain at least the actual obtainable CO_2 purity under the given adsorption−desorption conditions. They assessed the potential of a TSA cycle based on the usage of the recovered product as regeneration purge gas by means of three different TSA cycles: (1) regeneration by indirect heating, (2) regeneration by indirect heating followed by hot product gas purge and (3) regeneration by hot product gas purge only. During cycle 1 (preliminary cycle), they determined the product purity that can be obtained at the given adsorption conditions and regeneration temperatures. In cycle 2, they introduced a hot product gas as purge stream before cooling and after indirect heating step and finally in cycle 3, bed regeneration is achieved by a direct contact with a hot product gas only. Thus, indirect heating of the bed is avoided. The hot purge gas composition is the same as the purity achieved in cycle 1 [48].

When using hot purge gas during desorption step, it is generally required a significant volume of hot gas to heat the bed due to the low heat capacity of the gases. This leads to the desorption of the adsorbate diluted in the heating gas, which becomes a problem since carbon dioxide must be recovered as pure as possible for transport and storage reasons. As a possible solution to this inconvenient, in case the adsorbent be an electrical conductor, an ‘‘in-situ’’ heating

by Joule effect has been proposed; in this process, an electrical current is applied directly to the packed bed. This is the concept of electrical swing adsorption (ESA) [46]. One shortcoming inherent of ESA principle when compared to TSA is the fact that the increase in temperature is accomplished by using electric power while in the case of TSA waste heat can be used. Ribeiro (2013) studied the potential use of ESA for CO_2 removal on gaseous streams and concluded that despite ESA may be considered a promising process to employ in CO_2 capture, however, the development of materials with enhanced adsorption properties and suitable electrical behavior is required. He also concluded that applying higher electric power for heating, enhances desorption rate and that the usage of N_2 purge flowrate during desorption has a strong influence in the CO_2 recovered amount purity.

Raganati *et al* (2016) evaluated the subsequent effect of heating and purging in a TSA process in a sound assisted fluidized bed on the CO_2 recovery efficiency. They concluded that this regeneration strategy offered similar advantages as traditional indirect heating methodologies, however, preventing some shortcomings from other technological alternatives, e.g., the necessity of adsorbents with specific electric conductivity as in ESA. They suggested as well that moderate desorption temperatures, namely 130°C, are suitable for CO_2 recovery though a subsequent purge is necessary once full recovery is not accomplished only by heating.

Combinations of VSA/PSA and TSA have also been proposed. Wang *et al.* (2012) carried out an experimental and modeling investigation on post-combustion carbon dioxide capture using zeolite 13X-APG by hybrid VTSA process. They concluded that in the hybrid VTSA process, it is neither requisite to use a deeper vacuum degree for the adsorbents regeneration when compared with the conventional VSA process, nor requisite to use a relatively higher temperature for desorption when compared with the conventional TSA process. Therefore, the regeneration conditions of adsorbents in the hybrid VTSA process become gentler when compared with the cases in VSA and TSA processes, while the energy consumption and capture cost can be reduced. Moreover, if the VTSA process is retrofitted in the existed power plants with the utilization of the lower grade heating/cooling sources, it will be a technical–economical adsorption process for post-combustion CO_2 capture.

Song *et al.* (2016) integrated chemical heat transformer and pressure recovery to reduce energy requirement in an advanced pressure–temperature swing adsorption (PTSA) CO_2 capture process. They assessed the energy consumption of the proposed adsorption process in both

experimental and numerical study. The simulation results indicated that the energy consumption of the proposed PTSA process decreased to 1.18 MJ/kg CO_2 (approximately 40% that of the conventional PTSA process).

Several dynamic models have been proposed for CO_2 adsorption via fixed bed as reported in literature [53]. Dantas *et al* (2011) investigated the adsorption of CO_2 on zeolite 13X by experiments and simulations considering different adsorption temperature. They concluded that their model was suitable for designing PSA cycles to separate CO_2 -N_2 mixtures. Rios *et al* (2014) also evaluated CO_2 -N_2 separation but using commercial activated carbons and MOF Cu-BTC (BASF, Germany) through breakthrough experiments and simulations. They concluded that despite adsorbent Cu-BTC displayed the highest selectivity for CO_2 adsorption; activated carbon C141 (Carbomafra, Brazil) was more likely to exhibit a better PSA performance on post-combustion scenario given its selectivity and toleration to humid conditions.

In a recent work, Ben-Mansour *et al* (2018) developed a simulated TSA system with various stages, namely feeding, rinse, heating and cooling for separating a CO_2/N_2 mixture using Mg-MOF-74 as adsorbent. They assessed the regeneration phase (i.e. heating and cooling) adjusting the regeneration time to explore the performance improvement for the TSA process. Interestingly, their model validation was performed based on experimental data on literature [57] and their own experiments but only on breakthrough experiments. This fact suggests the existence of little available experimental data on the desorption step.

In summary, many approaches for CO_2 capture have been developed experimentally and/or by simulations using different regeneration strategies and multiples adsorbent materials. With regard to simulations, dynamic process modeling is necessary to predict the behavior of process variables when they are modified. In adsorption separation processes, the gas –solid equilibrium limits the separation capacity of the product of interest from the gas stream to the solid phase. In the same way, the equilibrium controls the dynamic behavior of the fixed bed since the Mass Transfer Zone (MTZ) nature is determined by the equilibrium isotherm. Once equilibrium is investigated, an appropriate mathematical model formulation, which contemplates all relevant transport phenomena (mass, energy and momentum) is required for a better understanding of the whole process dynamics [53].

3. EXPERIMENTAL

3.1. Materials

Helium (99.999 %), Carbon dioxide (99.98 %) and Nitrogen (99.999 %), used for the experiments, were supplied by White Martins Praxair Inc. (Brazil). The adsorbent used in this study is binderless zeolite 13X (NaX) supplied by Kostrolith (Germany) in bead form of 1.6 mm-2.5mm particle diameter.

3.2. Methodology

The methodology of this dissertation consisted of:

I. Adsorbent textural properties analysis.
II. Monocomponent and binary gas isotherms of CO_2 and N_2.
III. Breakthrough and desorption experiments.
IV. Breakthrough and desorption simulations.

3.2.1. Adsorbent Textural Properties

Autosorb IQ3 (Quantachrome, USA) was employed to build nitrogen adsorption-desorption isotherm at -196°C for material zeolite 13X. The data generated by the isotherm is used to determine the textural properties of the adsorbent (i.e., specific surface area, specific total pore volume and specific micropore volume).

A basic scheme useful to explain Autosorb IQ3 functioning is shown in Figure 9. The equipment essentially consists of gas input, a manifold, pressure transducers and a sample cell. The manifold is used to dose gas aliquots towards the sample cell where the adsorbent is placed during adsorption and to gradually remove gas from sample cell while desorbing. The operational principal of the equipment consists of measuring the pressure inside the manifold, which has a known volume value, before and after dosing the adsorptive towards the cell. The amount of gas adsorbed (n_{ads}) is calculated based on ideal gas law:

$$PV = n_{ads}R_gT \quad (4)$$

$$n_{ads} = n_{dosed} - n_{void} \quad (5)$$

$$n_{ads} = (\Delta PV/R_gT)_{manifold.} - (PV/R_gT)_{cell} \quad (6)$$

where P, V, R_g and T represent the pressure, volume, ideal gas constant and temperature respectively.

Figure 9. Basic scheme of Autosorb IQ3 (Quantachrome, USA).

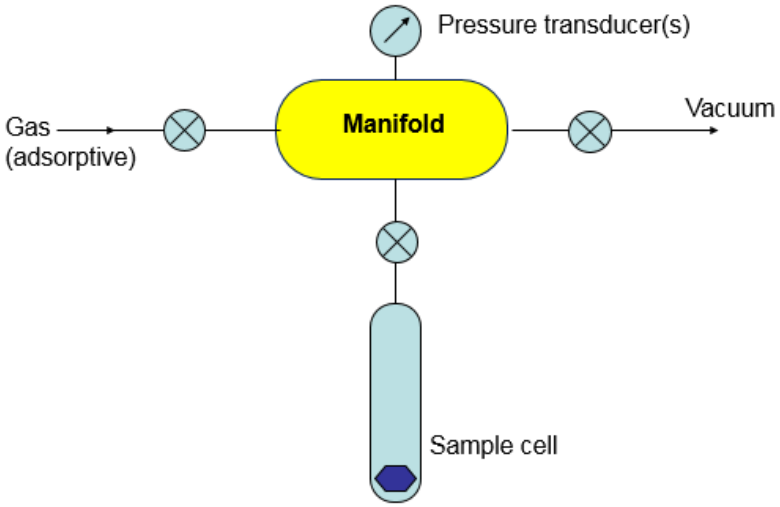

Source: Own authorship.

The difference between the dosed amount (n_{dosed}) (i.e., amount of gas driven into (adsorption) or out of (desorption) the cell by the end of an equilibration period.) and the amount of gas remaining unadsorbed (n_{void}) (i.e., in the void volume) is what it is considered adsorbed in the sample (n_{ads}).

The experimental procedure initiates with adsorbent material outgassing by means of heating and vacuum. Subsequently, a portion of adsorptive is admitted to build some target pressure in the manifold. The gas is later expanded from manifold into the cell sample and in time pressure equilibration is achieved. Final pressure is recorded and difference from initial manifold pressure ($\Delta P_{manifold}$) is used to determine the amount of gas dosed. The equipment automatically repeats this process at higher-pressure levels until reaching 95% of adsorptive relative pressure (P/P_o) where gas dosing is interrupted and desorption step is consequently started. In desorption, contrary to

adsorption, the gas is expanded from sample cell into manifold while the pressure increase in manifold is recorded for calculation purpose.

3.2.1.1. Specific Surface Area Evaluation

The traditional method to assess the specific surface area of porous materials is the Brunauer-Emmett-Teller (BET) method. BET method uses information derived from gas physisorption isotherm (e.g., N_2 at -196 °C, CO_2 at 0 °C or A_r at -186 °C), being nitrogen the most widely adsorptive employed for this purpose. The BET method firstly considers constructing the 'BET plot' ($\frac{(P/P_o)}{n[1-(P/P_o)]}$ vs. $\left[\frac{P}{P_o}\right]$) from gas physisorption data to obtain the specific monolayer capacity (n_m) following the linear form of BET equation:

$$\frac{(P/P_o)}{n[1-(P/P_o)]} = \frac{1}{n_m C} + \frac{C-1}{n_m C}\left[\frac{P}{P_o}\right] \quad (7)$$

where *C* represents an empirical constant (also called BET constant) and n represents the number of moles of gas adsorbed per material unit mass at relative pressure (P/P_o). The BET area (S_{BET}) is then calculated by including the appropriate adsorptive molecular cross sectional area (σ) (e.g., for N_2, σ=1,62E-19 m^2) in the monolayer and the number of molecules inside that sectional area represented by the Avogadro number (*L*) [21] as described in equation (8):

$$S_{BET} = n_m L \sigma \quad (8)$$

Since BET area value might change depending on the relative pressure range selected for 'BET plot' and eventually there can be several relative pressure ranges yielding a straight line, some criteria, detailed elsewhere [20], have been adopted to help obtain reliable results.

3.2.1.2. Total Pore Volume and Micropore Volume Evaluation

Adsorbent total pore volume (V_P) was estimated by turning gas moles adsorbed from gas physisorption data (n_{sat}) at almost vapor pressure saturation (i.e., $P/P_o \approx 0.995$) into total pore

volume by the aid of equation (9), assuming that complete pore filling is accomplished at that condition since liquid like adsorbate behavior is experienced. Nitrogen isotherm at -196 °C is largely used for this calculation.

$$Total\ pore\ volume, V_P\ (cm^3 g^{-1})\ = n_{sat}(mol g^{-1})\left(\frac{M}{\rho_L}\right) \quad (9)$$

with M representing adsorbate molar mass (e.g., for N_2 is ca 28.01 g.cm^{-3}) and ρ_L the adsorbate density at liquid state (e.g., for N_2 is ca 0.808 g.cm^{-3}). The total pore volume denotes the empty space within the material structure per adsorbent mass unit.

Analogous to total pore volume assessment, micropore volume (V_{mp}) is calculated from conversion of microporosity capacity (n_{mp}) also assuming adsorbate liquid state during pore filling:

$$Micropore\ pore\ volume, V_{mp}\ (cm^3 g^{-1})\ = n_{mp}(mol g^{-1})\left(\frac{M}{\rho_L}\right) \quad (10)$$

The estimation of n_{mp} is not straightforward since most microporous materials own significant external surface and mesopores, and micropore filling generally occurs at low relative pressures [21]. Therefore, various methods have been proposed for this determination based on physisorption isotherms from microporous materials. The Dubinin- Raduskevich (*D-R*) equation is extensively applied for this purpose and is generally expressed in the following manner:

$$log_{10}(n) = log_{10}(n_{mp}) - D log_{10}^2\left(\frac{P^0}{P}\right) \quad (11)$$

A plot of $log_{10}(n)$ against $log_{10}^2 (P_o/P)$ is expected to be linear with slope *D* (empirical constant) and intercept $log_{10}(n_{mp})$ according to *D-R* theory [23].

3.2.2. Gas Isotherms

Magnetic Suspension Balance (Rubotherm, Germany) equipped with an automatic gas-dosing unit and a binary gas mixer was used to carry out monocomponent and binary isotherms for

carbon dioxide (CO_2) and nitrogen (N_2). This balance operates by means of two measuring points allowing to additionally determinate the adsorbate density experimentally.

Single gas isotherms were performed at three temperatures: 25, 50, and 75 °C in a pressure range from 0 bar to 10 bar. Binary isotherm of CO_2-N_2 (15/85 % v/v) was also constructed at the same pressure range but solely at 50°C since this temperature represents post-combustion scenario for flue gas.

The mass of the gas adsorbed by the material (Δm) at an specific pressure (P_i) is not directly measured by the balance, instead, the total mass of components in the balance plus the adsorbent and gas adsorbed (m_i) are measured directly at every single point of pressure, so that these variables can be related as follows:

$$\Delta m = m_i - m_0 \tag{12}$$

where m_0 represents the total mass of the components in the balance with the outgassed adsorbent. The value of m_0 is calculated prior to isotherm experiments at the end of the outgassing step and represents the balance measurement at nearly zero pressure.

3.2.2.1. Gas isotherm measurement

The value of Δm depends on system pressure (P) and temperature (T) and must be corrected during experimental runs adding up the buoyancy effect (B_o), which is more evident at higher pressures:

$$m_{exc}(P,T) = \Delta m(P,T) + B_o\,(P,T) \tag{13}$$

where m_{exc} is usually known as the excess mass and B_o can be defined in the following way:

$$B_o = (V_b + V_s)\rho_g(P,T) \tag{14}$$

here V_b is the volume of the components in the balance without adsorbent, V_s is the solid (adsorbent) volume excluding internal pores and ρ_g is the gas (adsorbate) density.

Substituting equation (14) in (13) gives equation (15):

$$m_{exc}(P,T) = \Delta m(P,T) + (V_b + V_s)\rho_g(P,T) \quad (15)$$

which represents the experimental equation to determine the excess mass of adsorbate at a specific pressure and temperature. Equation (15) can be divided by the outgassed sample mass (m_{ads}) used in the experiment to obtain the equation (16) in grams per grams of adsorbent:

$$m_{exc}(P,T)(g/g) = \frac{\left[\Delta m(P,T) + (V_b + V_s)\rho_g(P,T)\right]}{m_{ads}} \quad (16)$$

In order to build the corresponding isotherm, the excess mass (m_{exc}) ($g.g^{-1}$) or as more commonly expressed (m_{exc}) ($mmol.g^{-1}$) must be calculated and then plotted against relative pressure (P/P_o) (being P_o the adsorptive saturation pressure) or simply pressure (P). The gas isotherm analysis was performed according to the experimental procedure explained elsewhere [58].

3.2.3. Breakthrough and Desorption Experiments

3.2.3.1. Conditioning before experiments

Prior to the adsorbent packing in the column, the material was reduced and sieved to 425µm -600µm particle diameter for better bed filling. Empty column and packed column weights were registered to calculate the packed mass of the material. The stainless steel column is cylindrical shape and its dimensions are 4.6 mm ID x 10 cm L.

3.2.3.2. Fixed Bed Laboratory Unit

The breakthrough and desorption experiments were carried out in a Fixed Bed Laboratory Unit (FBU) (Figure 10) consisting basically of two series-connected chromatographs coupled with:

I. Multi-loop valve (Model EMT2CST12MWE, Vici Valco Instruments Co, Inc., USA) owning 12 loops of 1 mL capacity.
II. Mass flow controllers (Model 840L-1-OV1-D-V1-S1, Sierra Instruments, Inc., USA).
III. Mass flow box (Model 954, Sierra Instruments, Inc., USA)

This unit is capable of:

- Constructing monocomponent and binary breakthrough curves of CO_2, N_2 and CH_4.
- Running dynamic adsorption-desorption experiments up to 400 °C.
- Performing isothermal adsorption and temperature programmed desorption.
- Performing gas purge desorption with the aid of Helium.

Figure 10-Fixed Bed Laboratory Unit (FBU)

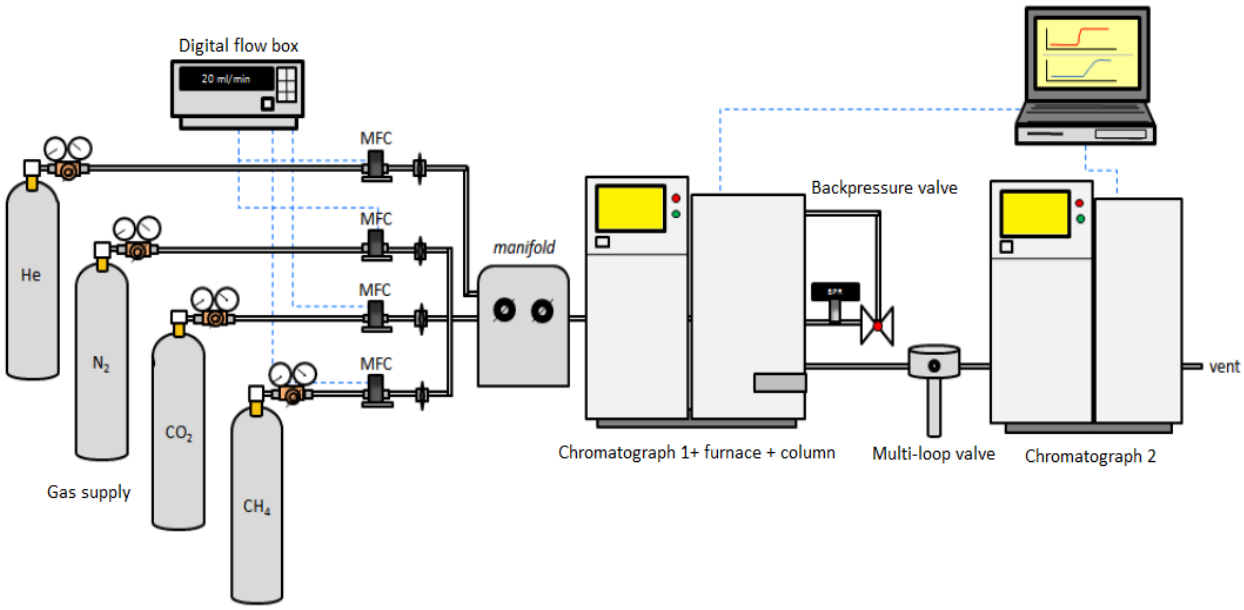

Source: Modified from [59]

The FBU possesses a unique column position located in the furnace of chromatograph 1 (Varian 450 GC, The Netherlands) on which the packed bed is placed and the temperature controlled adsorption-desorption tests occur. Gas mixtures were obtained by adjusting mass flow controllers at desired values set on the mass flow box always including Helium in the mixture since it is an equipment operational requirement. Multi-loop valve was used to capture portions of gas mixture (aliquots), at the exit of the column at programmed times, to be later analyzed in

chromatograph 2 (Varian 430 GC, The Netherlands) in order to generate the respective breakthrough curve. Aliquots were quantified by means of a Thermal Conductivity Detector (TCD) in chromatograph 2 sensing the difference in thermal conductivity between the analytes and the carrier gas (Helium in this case).

Once the column was placed inside the furnace of chromatograph 1, the adsorbent was outgassed for 8 h at 300 °C along with use of a Helium purge stream of approximately 8 cm^3min^{-1}, assuming the latter one as inert (i.e., nonadsorbed molecule). This procedure, generally known as the adsorbent regeneration, was executed for every run to guarantee the gas removal from the material pore structure. Afterwards the furnace was cooled off up to the experiment conditions to start the respective experimental run. To correlate the resulting peak areas from the chromatograms with the outlet gas concentration, a calibration curve was previously performed by analyzing several gas stream aliquots at the exit of the column after saturating the fixed bed. Once saturation was achieved, inlet and outlet gas concentrations are identical. Considering the inlet gas concentration a known value, then it was possible to generate a linear correlation to obtain the gas concentration at the outlet from chromatogram data.

3.2.3.3. Experiment outline

Experiment outline is summarized in Figure 11, which consisted of two stages: adsorption and desorption process. In adsorption experiments, single CO_2 breakthrough curve in presence of Helium at 50 °C was initially carried out to test FBU repeatability and accuracy. Afterwards, binary breakthrough curves of CO_2-N_2 in presence of Helium were performed at 25, 50 and 75 °C respectively. CO_2 represented 15 % (v/v) over the gas mixture simulating maximum concentration of this flue gas component in post-combustion scenario from coal-fired power plants. N_2 and He represented 75 % and 10 % in the gaseous mixture. Total volumetric gas flow entering the column during adsorption step was set to be 80 cm^3min^{-1} STP for all runs.

The desorption process was carried out to assess CO_2 recovery in two scenarios:

- *Regeneration by He purge and then temperature swing along with He purge (configuration 1):* In this scenario, desorption was firstly performed only with an 80cm^3min^{-1} STP He purge until either no CO_2 or the lowest CO_2 signal concentration was detected by the TCD.

Temperature is maintained constant during He purge step and is the same of that in the adsorption step. Subsequently, the system temperature was increased until reaching the desired regeneration temperature preserving the same He purge flowrate. Several regeneration temperatures were tested to investigate the influence of this parameter in CO_2 recovery as displayed in the experiment outline sequence in Figure 11. The desorption process was again considered completed when CO_2 concentration was no longer detected by the TCD. Figure 12 exemplifies a typical normalized concentration profile for CO_2-N_2 binary system in the whole adsorption-desorption process according to the experimental sequence outline.

Figure 11. Experiment outline sequence.

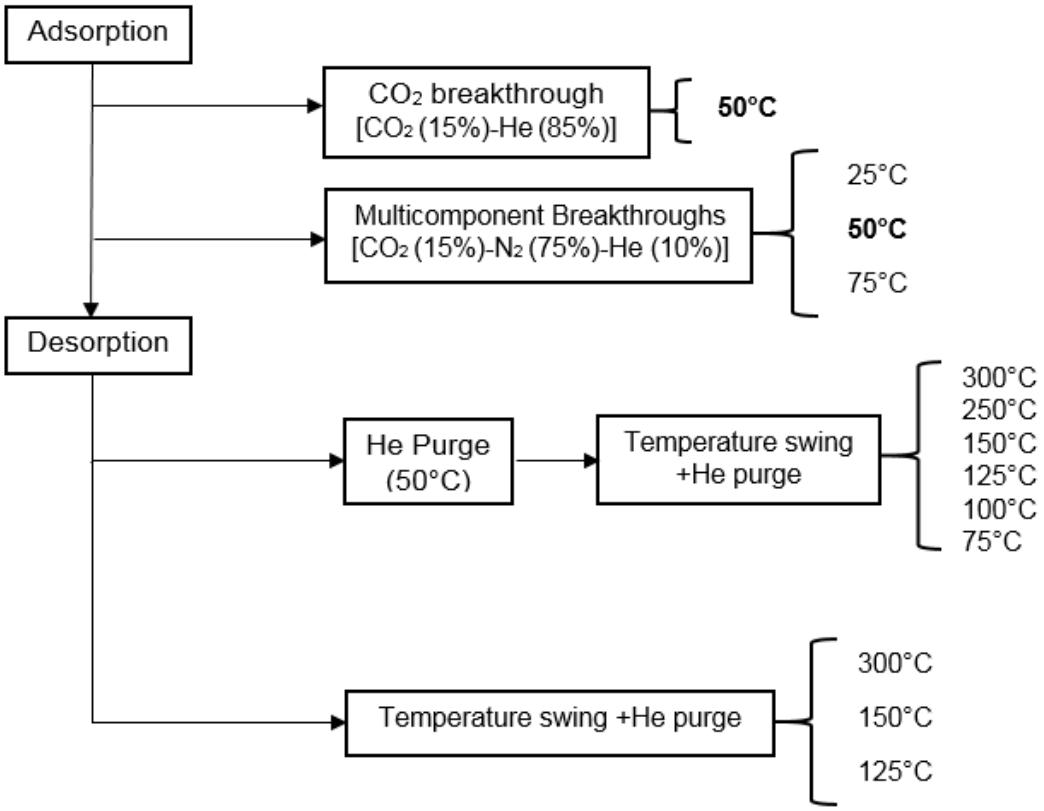

Source: Own authorship

- *Regeneration by temperature swing along with He purge (configuration 2)*: In this case, the initial He purge step is omitted. Instead, desorption is executed immediately by temperature increase accompanied by an 80 cm^3min^{-1} STP He purge as can be appreciated in Figure 13. The regeneration temperatures employed in the experiments were 300, 150 and 125 °C. The

reason why the number of temperatures was reduced in comparison with the first scenario will be explained in the results section.

All desorption tests were exclusively performed after adsorption at 50 °C since flue gas temperature is usually between 40 and 60 °C [6, 60]. All desorption experiments started from saturation point and when applying temperature swing, a 20 °C.min^{-1} temperature ramp was adjusted.

Figure 12. Normalized concentration profile for CO_2 and N_2 in adsorption/desorption process. Regeneration by He purge + (Temperature swing + He purge).

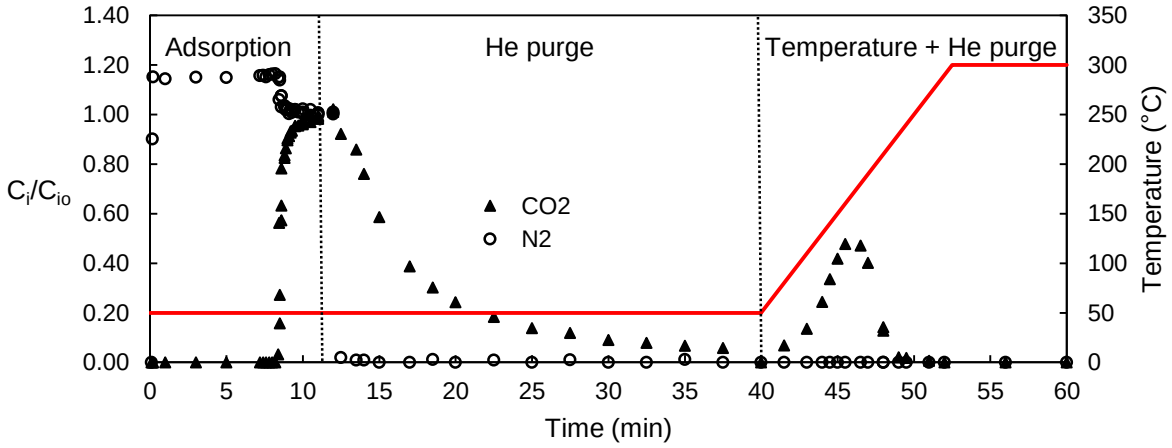

Source: Own authorship

Figure 13. Normalized concentration profile for CO_2 and N_2 in adsorption and desorption process. Regeneration by (Temperature swing + He purge).

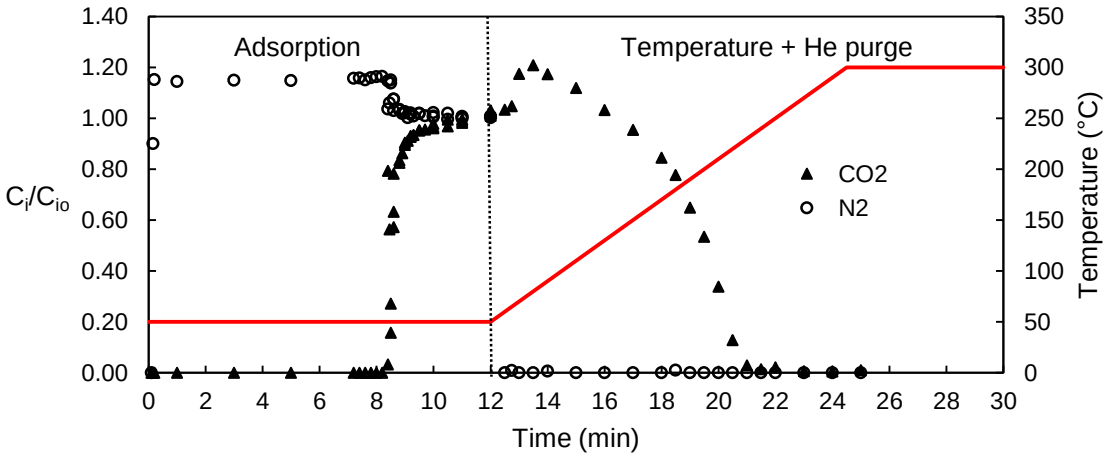

Source: Own authorship

3.2.3.4. Fixed bed capacity

An important parameter to be considered in breakthrough experiments is the stoichiometric time (t_{st}). Stoichiometric time may be calculated as follows [45]:

$$t_{st} = \int_0^{te} \left(1 - \frac{C_i}{C_{i0}}\right) dt \tag{17}$$

The stoichiometric time is independent of dispersion in the MTZ whereas breakthrough time (t_b) and saturation time (t_e) can fluctuate due to dispersion (i.e., for the same system and conditions, stoichiometric time shall remain invariable no matter how dispersive the MTZ could be).

In order to calculate the adsorbed quantity of a component i at time t from the breakthrough experiments data, a mass balance in the fixed bed by integral formulation may be applied:

$$Moles\ of\ component\ i|_{inlet} - Moles\ of\ component\ i|_{outlet} = Moles\ of\ component\ i\ accumulated\ in\ gaseous\ and\ adsorbed\ phase$$

$$\int_0^t QC_{i0}dt - \int_0^t QC_i dt = \varepsilon V_{col} C_{i0} + m_{ads}\bar{q}_i \tag{18}$$

Here Q is the volumetric flow, C_{i0} and C_i represents the concentration of component i in the gas phase at inlet and outlet respectively, ε is the bed porosity, V_{col} is the column volume, m_{ads} is the outgassed adsorbent mass value and finally $\bar{q}_i$ denotes the concentration of component i in the adsorbed phase. Isolating $\bar{q}_i$ in equation (18), we obtain:

$$\bar{q}_i = \frac{C_{i0}}{m_{ads}}\left[Q\int_0^t \left[1 - \frac{C_i}{C_{i0}}\right] dt - \varepsilon V_{col}\right] \tag{19}$$

When considering the bed capacity, the upper limit t, in equation (19) integral, becomes saturation time (t_e). Therefore, the value of the integral in the former equation represents the stoichiometric time (t_{st}):

$$\bar{q}_i = \frac{C_{i0}}{m_{ads}}[Q t_{st} - \varepsilon V_{col}] \tag{20}$$

Equation (20) may be more convenient if the inlet gas concentration (C_{i0}) is transformed in terms of component pressure (P_i) and temperature (T) by the aid of the ideal gas law to obtain equation (21):

$$\bar{q}_i = \frac{P_i}{R_g T m_{ads}}[Q t_{st} - \varepsilon V_{col}] \tag{21}$$

If the number of moles adsorbed is desired to be calculated, equation (15) can turn into equation (16) by multiplying the mass of the adsorbent:

$$n_{ads} = \bar{q}_i m_{ads} = \frac{P_i Q t_{st}}{R_g T} - \frac{\varepsilon P_i V_{col}}{R_g T} \tag{22}$$

Here at the right side of equation (16), the first term refers to the number of retained moles in the column (n_r) and the second term refers to the number of moles in the fluid phase (n_f) (i.e., moles contained in the bed porosity):

$$n_{ads} = n_r - n_f \tag{23}$$

In case of a binary experiment, as represented in Figure 14, the number of moles of compound 1 (weakly adsorbed) retained in the bed is equivalent to the area A minus the roll-up area OS. For the compound 2 (strongly adsorbed), the number of moles retained in the fixed bed equals area A plus area B [61].

The number of moles desorbed can simply be calculated by integrating the molar flux profile as a function of time for each component in the mixture during desorption.

Figure 14. Binary breakthrough example

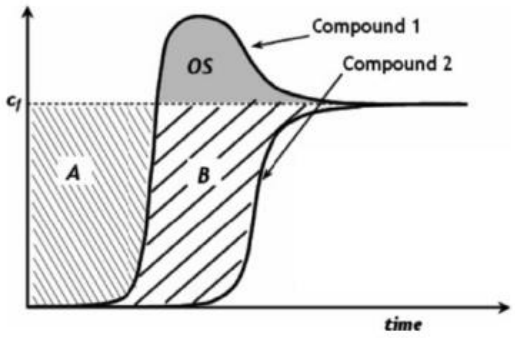

Source: [61]

3.2.3.5. Dead volume for experimental time correction

Dead volume is generally referred as to that portion of the FBU volume that is contact with the gas molecules during an experimental run excluding the adsorbent bed. The dead volume is a constant parameter for a specific system and its calculation is highly important to determine accurately the fixed bed capacity from breakthrough experiments. Once stoichiometric time is derived, it shall be corrected subtracting the time the gas flows from supply to column inlet (Δt_o) and the time from column exit to the analyzer (Δt_1) as shown in Figure 15.

Figure 15. Dead volume and dead time system scheme.

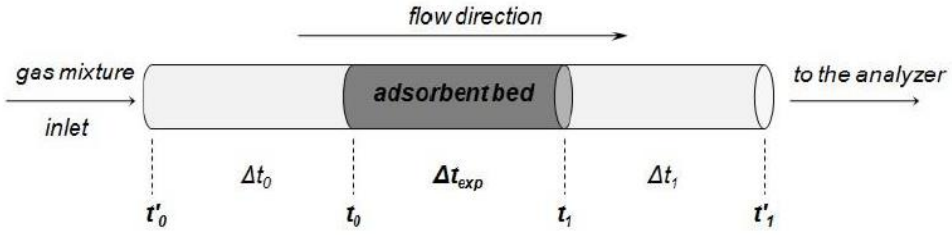

Source: [62]

This dead time ($\Delta t_o+\Delta t_1$) is related to dead volume (V_d) and varies with pressure and volumetric flow (Q). If one assume constant atmospheric pressure throughout the system piping, then, the dead time may be calculated by equation (24).

$$\Delta t_0 + \Delta t_1 = \frac{V_d}{Q} \quad (24)$$

The dead volume calculation might be carried out by the aid of a random breakthrough curve with empty column, so that, the time taken by the gas to flow through the whole system will represent the dead time for the volumetric flow value employed in the experiment.

Figure 16. CO_2 breakthrough curve for dead volume calculation

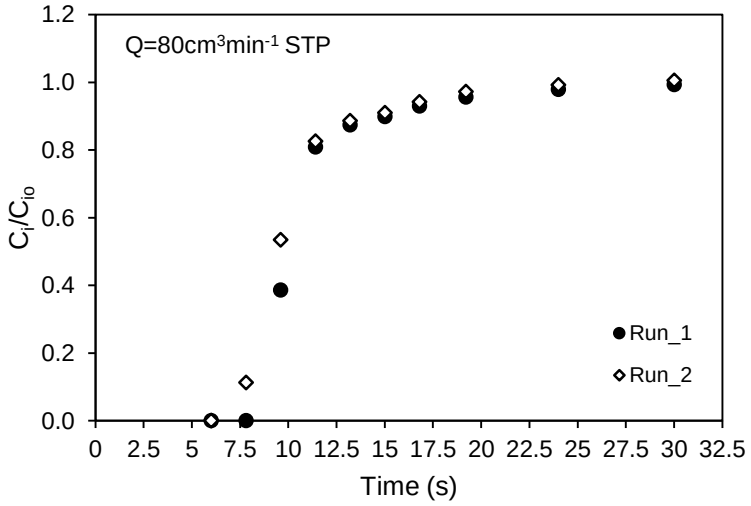

Source: own authorship

For this purpose, a gaseous stream of CO_2 (15 % v/v) diluted in helium was used to yield the breakthrough curve for dead volume calculation as presented in Figure 16. From Figure 16, one can also infer that the dead time is ca 7.8 s, once the curve starts to break at this point. Then, applying equation (24), the dead volume can be calculated. The preceding dead volume value shall be corrected subtracting the column volume as shown in Table 2.

Table 2. Dead volume for FBU

Q ($cm^3.min^{-1}$)	$\Delta t_o+\Delta t_1$ (s)	V_d+V_{col} (cm^3)	V_{col} (cm^3)	V_d (cm^3)
80	7.8	10.4	0.8	9.6

Source: own authorship

3.2.4. Breakthrough and Desorption simulations

The proposed mathematical model to run the simulations is described in the section 4 of this dissertation.

4. MATHEMATICAL MODEL FORMULATION

A modeling formulation was developed to efficiently simulate adsorption-desorption process of the CO_2-N_2 binary system. The mathematical framework included detailed fixed bed adsorption process by: i) Partial Differential and Algebraic Equations (PDAEs) describing transport phenomena in the gas phase (i.e., mass, heat and momentum balance), ii) mass transfer particle balance iii) adsorption isotherm models, iv) equation of state for the fluid phase, v) physical properties of both gas mixture and fixed bed and vi) transport parameters of the gas mixture.

The mathematical model equations were derived based on the following assumptions:

- The gas mixture follow the ideal gas equation of state.
- The fluid transport pattern through the bed is axially dispersed.
- Radial direction gradients of any property are neglected.
- A linear driving force (LDF) model describes the mass transport kinetics in the particle.
- Immediate thermal equilibrium between the gas and the solid phased is considered.
- The system operates in non-isothermal and non-adiabatic conditions.
- The physical properties of the adsorbent and the column wall are considered invariable.

4.1. Mass Balance

The fluid phase mass balance was applied in an arbitrary control volume ($A\Delta z$) within the fixed bed. In this case, the mass flux (F_m) per cross sectional area (A) of the column goes through a small bed length fraction (Δz) as seen in Figure 17. The mass balance was accomplished by differential formulation as follows:

$$Mass\ Flux_{in} - Mass\ Flux_{out} = Mass\ accumulation$$

$$\varepsilon A F_m|_z - \varepsilon A F_m|_{z+\Delta z} = A\Delta z \frac{\partial C_i}{\partial t} \tag{25}$$

Dividing between ε$A\Delta z$ and applying limit function when $\Delta z \rightarrow 0$:

$$-\frac{\partial F_m}{\partial z} = \frac{1}{\varepsilon}\frac{\partial C_i}{\partial t} \tag{26}$$

here, C_i (mol/m^3) represents total concentration of component *i* in system and ε is the bed porosity.

Figure 17. Fixed bed scheme

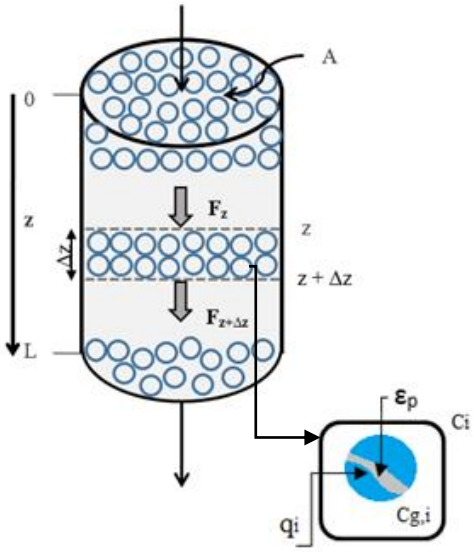

Source: own authorship.

The total concentration (C_i) in the accumulation term of equation (26) can be defined as follows:

$$C_i = \left[\varepsilon C_{g,i} + (1-\varepsilon)(\varepsilon_p C_{g,i} + \bar{q}_i)\right] \tag{27}$$

Once the portion of the inlet flux gas, that accumulates in control volume, is distributed within the bed porosity, inside the particle porosity and on the material surface in adsorbed phase. In equation (27), C_{gi} represents the concentration of component i in the gaseous phase in both the bed porosity and particle porosity, $\bar{q}_i$ embodies the concentration of component i in the solid (adsorbed phase) and ε_p is the particle porosity.

Hence, substituting equation (27) in equation (26):

$$-\frac{\partial F_m}{\partial z} = \frac{\partial C_{g,i}}{\partial t} + \frac{(1-\varepsilon)}{\varepsilon}\varepsilon_p \frac{\partial C_{g,i}}{\partial t} + \frac{(1-\varepsilon)}{\varepsilon}\frac{\partial \bar{q}_i}{\partial t} \tag{28}$$

Now F_m can be split into a convective flux contribution and a dispersive flux contribution respectively in the following way:

$$F_m = uC_{g,i} + F_{dispersive} \tag{29}$$

here u represents intersticial velocity. The dispersive flux ($F_{dispersive}$) can be expressed in terms of axial mass dispersion (D_{ax}) analogous to Fick's First Law:

$$F_{dispersive} = -D_{ax}\frac{\partial C_{g,i}}{\partial z} \tag{30}$$

Replacing equation (30) in equation (29) gives us:

$$F_m = -\left[D_{ax}\frac{\partial C_{g,i}}{\partial z} - uC_{g,i}\right] \tag{31}$$

Then applying partial derivation in equation (31):

$$-\frac{\partial F_m}{\partial z} = \left[D_{ax}\frac{\partial^2 C_{g,i}}{\partial z^2} - \frac{\partial}{\partial z}(uC_{g,i})\right] \tag{32}$$

Finally substituing equation (32) in equation (28), we obtain:

$$D_{ax}\frac{\partial^2 C_{g,i}}{\partial z^2} - \frac{\partial}{\partial z}(uC_{g,i}) = \frac{\partial C_{g,i}}{\partial t} + \frac{(1-\varepsilon)}{\varepsilon}\varepsilon_p \frac{\partial C_{g,i}}{\partial t} + \frac{(1-\varepsilon)}{\varepsilon}\frac{\partial \bar{q}_i}{\partial t} \tag{33}$$

Rearranging, we have:

$$-\varepsilon D_{ax}\frac{\partial^2 C_{g,i}}{\partial z^2}+\frac{\partial}{\partial z}\left(vC_{g,i}\right)+\varepsilon\frac{\partial C_{g,i}}{\partial t}+(1-\varepsilon)\varepsilon_p\frac{\partial C_{g,i}}{\partial t}+(1-\varepsilon)\frac{\partial \overline{q_i}}{\partial t}=0 \quad (34)$$

Or

$$-\varepsilon D_{ax}\frac{\partial^2 C_{g,i}}{\partial z^2}+\frac{\partial}{\partial z}\left(vC_{g,i}\right)+\varepsilon\frac{\partial C_{g,i}}{\partial t}+(1-\varepsilon)\varepsilon_p\frac{\partial C_{g,i}}{\partial t}+(1-\varepsilon)\rho_p\frac{\partial \overline{q_i}}{\partial t}=0 \quad (35)$$

where $\overline{q_i}$ is in mol/Kg of adsorbent, ρ_p represents the particle density and v is the superficial velocity.

As a general rule, all properties varying with length (z) require boundary conditions (BCs). The number of BCs is equal to the order of the partial derivation applied to that variable. On the other hand, all properties varying with time (t) require an initial condition (IC).

Equation (35) is consequently subjected to the following BCs and ICs:

- Boundary conditions (at Z=0): Gas concentration is equal right before inlet (Z=0-) and inmediately after inlet (Z=0+) (i.g., $C_{g,i}(0-)=C_{g,i}(0+)$). Then if a mass balance at inlet is perfomed, we have :

$$vC_{g,i}\big|_{inlet}=vC_{g,i}\big|_{z=0}$$

The same boundary condition in terms of the total gas concentration (C_g) is necessary to specificate superficial velocity:

$$vC_g\big|_{inlet}=vC_g\big|_{z=0}$$

where $C_g=\sum_{i=1}^{NoC}C_{g,i}$

- Boundary condition (at Z=L): Continuous gas concentration profile is experienced at column exit (i.g., $C_{g,i}(L-)=C_{g,i}(L+)$). Therefore, no concentration changes are exhibited at the outlet.

$$\frac{\partial C_{g,i}}{\partial z} = 0\Big|_{z=L}$$

- Initial conditions (at t=0): while the bed is being regenerated, CO_2 and N_2 concentrations in the gas and adsorbed phase are zero.

$$C_{g,i} = \overline{q_i} = 0\Big|_{t=0}$$

The average adsorbed concentration $\overline{q_i}$ needs to be specified by another equation once it is an unknown value in equation (35). A material balance around a spherical particle with its corresponding boundary conditions is normally applied to calculate $\overline{q_i}$. The mathematical models that represent the particle balance are generally known as mass transfer resistance or diffusion models. However, despite the accuracy these models exhibit, due to the complexity in solving these equations, simplified correlations able to describe with good approximation this type of models have been adopted using an expression that involves the rate of adsorption of particles (i.e. kinetics) without the use of spatial coordinates. The most well-known model is the LDF (Linear Driving Force) that was first proposed by Glueckauf and Coates in 1947. Glueckauf and Coates suggested that the rate of adsorption of an adsorbate on the adsorbent particles is proportional to the linear difference between the concentration of that adsorbate on the external surface of the particle (adsorption equilibrium concentration, $q_{e,i}$) and its mean concentration inside the particle (amount of average adsorption by volume, $\overline{q_i}$) [54] .

$$\frac{\partial \overline{q_i}}{\partial t} = K_{LDF}(q_{e,i} - \overline{q_i}) \tag{36}$$

where K_{LDF} is the LDF model mass transfer coefficient. Glueckauf demonstrated that for spherical particles, the K_{LDF} coefficient can be defined in the following way:

$$K_{LDF} = \frac{15 D_{e,i}}{r_p^2} \tag{37}$$

where $D_{e,i}$ and r_p^2 represent the effective diffusivity of component *i* and the particle radius respectively. Several correlations are available in the literature to calculate the effective diffusivity as reported by Shafeeyan *et al* (2014) on their review of mathematical modeling of fixed-bed columns for CO_2 adsorption. However, the K_{LDF} coefficient can also be contemplated as an adjustable parameter [63]. In consequence, for a better simulation accuracy, the K_{LDF} coefficient was adjusted to the breakthrough or desorption experimental data in this research.

4.2. Energy Balance

The energy balance is similarly applied in an arbitrary control volume as in the mass balance. In this case, aside from the energy flux (F_e) going through the cross sectional area of the column, there is energy generation and energy removal within the control volume as stated below:

$$Energy\ accumulation\ = Energy\ Flux_{in} - Energy\ Flux_{out}\ \pm Energy_{generation/removal}$$

$$\varepsilon A \Delta z \frac{\partial E}{\partial t} = \varepsilon A F_e|_z - \varepsilon A F_e|_{z+\Delta z} + (G - R)\varepsilon A \Delta z \tag{38}$$

The energy generation (*G*) and energy removal (*R*) terms are owed to the heat derived from adsorption phenomenon and the energy loss by energy transfer between the gas and the wall, and they can be defined in the following manner:

$$G = \rho_b(-\Delta H)\frac{\partial \bar{q}}{\partial t} \tag{39}$$

$$R = \frac{4h_w}{d_i}(T_g - T_w) \tag{40}$$

where *(-ΔH)* represents the isosteric heat of adsorption, h_w is the heat transfer coefficient between the gas, the wall and T_g and T_w are the gas temperature and the wall temperature respectively and d_i is the internal column diameter.

Dividing equation (1) between $\varepsilon A \Delta z$ and applying limit function when $\Delta z \rightarrow 0$, we obtain:

$$\frac{\partial E}{\partial t} = -\frac{\partial F_e}{\partial z} + (G - R) \tag{41}$$

The Energy flux (F_e), as in the mass balance, also consists of a dispersive and a convective flux as represented below:

$$F_e = \begin{cases} F_{convective} = vCC_{vg}T_g \\ F_{dispersive} = -\lambda_e \dfrac{\partial T_g}{\partial z} \end{cases}$$

Here C denotes concentration; C_{vg} is the gas calorific capacity at constant volume (in molar basis) and λ_e is the heat axial dispersion coefficient.

Therefore, the partial derivative of F with respect to length (z) is

$$\frac{\partial F}{\partial z} = \left[\frac{\partial}{\partial z}\left(vCC_{vg}T_g\right) - \frac{\partial}{\partial z}\left(\lambda_e\left(\frac{\partial T_g}{\partial z}\right)\right)\right] \tag{42}$$

The total energy per volume unit (E) is a sum of kinetic (E_k), potential (E_p) and internal energy (U). Kinetic and potential energy can be neglected in this case since internal one mainly produces addition of energy in the system (i.e., $U >> E_k, E_p$). Thus,

$$E = U \tag{43}$$

Per definition, the internal energy U can be expressed as:

$$U = H - PV \tag{44}$$

where H represents the enthalpy and P, V the pressure and volume respectively.

The system total energy (E) takes into account energy changes in both the gas and the solid phases. Consequently, one can quantify these two contributions in the control volume (V) as follows:

$$E = \begin{cases} E_{gas} = U_{gas} = \dfrac{H - P^{gas}V}{V} = CC_{pg}T_g - P^{gas} = CC_{pg}T_g - \left[\varepsilon + (1-\varepsilon)\varepsilon_p\right]P & (45) \\ E_{solid} = U_{solid} = \dfrac{H}{V} = \rho_s C_{ps} T_s & (46) \end{cases}$$

where C_{pg} and C_{ps} denote the calorific capacity at constant pressure (in molar basis) for the gas and the solid phase respectively and ρ_s and T_s are the solid density and temperature.

For the solid phase, the pressure effect can be neglected as one can see in equation (46), while in the gas phase is the sum of the impact of the gas pressure in both the interparticle and the intraparticle void volume. One can also consider energy equilibrium between the gas and solid phase ($T_s = T_g$), so that no further energy balance in the solid is necessary.

Concentration (C) in equation (45) can be defined in the same way as in equation (27):

$$C = \left[\varepsilon C_g + (1-\varepsilon)(\varepsilon_p C_g + \rho_p \bar{q})\right] \quad (47)$$

Then, the energy accumulation term in equation (4) can be written as described below:

$$\frac{\partial E}{\partial t} = \frac{\partial}{\partial t}\left[\varepsilon C_g + (1-\varepsilon)(\varepsilon_p C_g + \rho_p \bar{q})\right] C_{pg} T_g - \left[\varepsilon + (1-\varepsilon)\varepsilon_p\right]\frac{\partial P}{\partial t} + \frac{\partial}{\partial t}(\rho_s C_{ps} T_g) \quad (48)$$

Replacing equations (39), (40), (42) and (48) in equation (41), we finally obtain equation (49):

$$\begin{aligned} &\frac{\partial}{\partial t}\left[\varepsilon C_g + (1-\varepsilon)(\varepsilon_p C_g + \rho_p \bar{q})\right] C_{pg} T_g - \left[\varepsilon + (1-\varepsilon)\varepsilon_p\right]\frac{\partial P}{\partial t} + \frac{\partial}{\partial t}(\rho_s C_{ps} T_g) \\ &+ \frac{\partial}{\partial z}\left(v C_g C_{vg} T_g\right) - \frac{\partial}{\partial z}\left(\lambda_e \left(\frac{\partial T_g}{\partial z}\right)\right) - \rho_b(-\Delta H)\frac{\partial \bar{q}}{\partial t} + \frac{4h_w}{d_i}(T_g - T_w) = 0 \end{aligned} \quad (49)$$

For mixtures, the equation (49) might be written as:

$$\frac{\partial}{\partial t}\left[\varepsilon C_g C_{pg} + (1-\varepsilon)(\varepsilon_p \sum C_{g,i} C_{pg,i} + \rho_p \sum \overline{q_i} C_{pg,i})\right] T_g - \left[\varepsilon + (1-\varepsilon)\varepsilon_p\right]\frac{\partial P}{\partial t} + \frac{\partial}{\partial t}(\rho_s C_{ps} T_g) + \frac{\partial}{\partial z}(v C_g C_{vg} T_g) - \frac{\partial}{\partial z}\left(\lambda_e \left(\frac{\partial T_g}{\partial z}\right)\right) - \rho_b \sum(-\Delta H_i)\frac{\partial \overline{q_i}}{\partial t} + \frac{4h_w}{d_i}(T_g - T_w) = 0 \quad (50)$$

An equation of state is necessary to correlate the concentration with system pressure and temperature. Since working pressure is very low (i.e., ca atmospheric pressure), hence, ideal gas law is suitable for this purpose:

$$P = C_g R_g T_g \quad (51)$$

Since the wall temperature (T_w) is an unknown value in equation (50), an energy balance at the column wall shall be provided taking into account both the energy transfer between the gas phase and the wall and the energy transfer between the wall and the surrounding air, as described by equation (52) as follows:

$$\rho_w C_{pw} \frac{\partial T_w}{\partial t} = \alpha_w h_w (T_g - T_w) - \alpha_{wl} U_o (T_w - T_{air}) \quad (52)$$

where ρ_w and C_{pw} refer to the density and the calorific capacity of the column wall, U_o represents the overall heat transfer coefficient between the column wall and the external air. T_{air} represents the external air temperature, α_w is the ratio of the internal surface area to the volume of the column wall and α_{wl} denotes the ratio of the logarithmic mean surface area of the column shell to the volume of the column.

The energy balance is subjected to the following BCs and ICs:

- Boundary condition (at *Z=0*): The convective energy flux entering the column is the same right where the column begins.

$$v C_{pg,i} C_{g,i} T_g\big|_{inlet} = v C_{pg,i} C_{g,i} T_g\big|_{z=0}$$

- Boundary condition (at *Z=L*): Continuous gas temperature is experienced at the column outlet.

$$\frac{\partial T_g}{\partial z} = 0\Big|_{z=L}$$

- Initial conditions (at t=0): At the beginning of the experiment, the gas, the wall and the sourrounding temperature are considered the same as the targeted adsorption temperature.

$$T_g = T_w = T_{air} = T_{ads}$$

4.3. Momentum Balance.

The pressure drop in packed beds is usually described by Ergun's equation (equation (53)), which is a combination of Blake-Kozeny and Burke-Plummer equations. As already addressed in this work, since working pressure is slightly over atmospheric pressure, the system is not expected to undergo drastic pressure drops. Despite that, in light of the rigurosity of the model, its use is essential to describe the pressure axial variation within the fixed bed.

$$-\frac{\partial P}{\partial z} = 150\frac{\mu_g(1-\varepsilon)^2}{\varepsilon^3 d_p^2}v + 1.75\frac{(1-\varepsilon)}{\varepsilon^3 d_p}\rho_g v^2 \qquad (53)$$

where μ_g is the gas mixture viscosity, d_p is the particle diameter and ρ_g is the gas mixture density.

The momentum balance is subjected to the following BC:

- Boundary condition (at Z=L): The pressure at the outlet of the column is the same as the atmospheric pressure.

$$P = P_{atm}|_{z=L}$$

4.4. Parameters determination

The solution of the entire mathematical model formulation requires the determination of several parameters. Most of these parameters were considered constant through the bed length

and have been either estimated by equations/correlations, measured experimentally or referenced from the literature.

4.4.1. Particle and bed parameters

The bed density, also called packing density, simply relates the mass of the regenerated adsorbent (m_{ads}) packed in the column with the column volume (V_{col}). The particle density and the solid density are calculated by the previous estimation of the specific solid volume ($\hat{V}_s$) and the specific pore volume ($\hat{V}_p$) of the sample from the Helium test. The particle density takes into account the whole particle volume including internal pore volume while the solid density only bears in mind the solid skeletal volume excluding the internal pore volume. The way of calculation of these and other bed/particle parameters are listed in Table 3.

Table 3. Particle and bed parameters.

Parameter	Symbol	Equation	Reference
Bed density	ρ_b	$\rho_b = \frac{m_{ads}}{V_{col}}$	-
Particle density	ρ_p	$\rho_p = \frac{1}{\hat{V}_s + \hat{V}_p}$	-
Solid Density	ρ_s	$\rho_s = \frac{1}{\hat{V}_s}$	-
Bed porosity	ε	$\varepsilon = 1 - (\hat{V}_s + \hat{V}_p)\rho_b$	-
Particle porosity	ε_p	$\varepsilon_p = 1 - \left(\frac{\hat{V}_s}{\hat{V}_s + \hat{V}_p}\right)$	-
Wall density	ρ_w	Value obtained in literature	[64]

Source: own authorship.

4.4.2. Mass transfer parameters

Mass transfer parameters were estimated via correlations as specified in Table 4. The mass axial dispersion coefficient of the gas mixture (D_{ax}) was calculated from the single gas component $D_{ax,i}$ values and their molar fractions (y_i) at the feeding conditions. The values of the

molecular diffusivity ($D_{m,i}$) of each gas in the mixture, the particle radius (r_p) and the inlet superficial velocity (v^{inlet}) were necessary to determine $D_{ax,i}$.

The binary diffusivity (D_{ij}) for each couple of the gas ternary mixture (CO_2-N_2-He) was also estimated. The definition and calculation of all parameters in the Chapman- Enskog equation for D_{ij} are detailed elsewhere [65].

Table 4. Mass transfer parameters.

Parameter	Symbol	Equation	Auxiliary equation	Reference
Mass axial dispersion coefficient	D_{ax}	$D_{ax} = \sum_{i=1}^{NoC} y_i D_{ax,i}$	$D_{ax,i} = (0.45 + 0.55\varepsilon)D_{m,i} + 0.35 r_p v^{inlet}$	[38]
Molecular diffusivity	$D_{m,i}$	$D_{m,i} = \frac{1 - y_i}{\sum_{\substack{j=1 \\ j \neq i}}^{NoC} \frac{y_j}{D_{ij}}}$	-	[38]
Binary diffusivity	D_{ij}	$D_{ij} = 0.0018583 \frac{\left[T^3 \left(\frac{1}{M_i} + \frac{1}{M_j}\right)\right]^{1/2}}{P \sigma_{ij}^2 \Omega_{D,ij}}$	-	Chapman-Enskog [65]

Source: own authorship.

4.4.3. Energy transfer parameters

The energy transfer parameters are listed in Table 5. The isosteric heat of adsorption for each gas mixture component was calculated by means of Clausius-Clapeyron equation from isotherm data of three temperatures. The heat axial dispersion coefficient (λ_e) was estimated via correlation using some dimensionless number values (Reynolds number, Prandtl number) and the gas thermal conductivity. The gas mixture thermal conductivity (K_g) was estimated from single gas component thermal conductivities ($K_{g,i}$) at feeding conditions. The dimensionless parameter $\emptyset_{ij}$ in K_g equation is the same as in the viscosity equation and will be further explained in the momentum parameter section.

The heat transfer coefficient between the gas and the wall (h_w) was calculated using a correlation. The overall heat transfer coefficient was estimated via resistance like equation combining convective and conductive heat transfer contributions. The wall heat conductivity (K_w) was obtained from literature [64].

Table 5. Energy transfer parameters

Parameter	Symbol	Equation	Auxiliary equation	Reference
Heat of adsorption	$(-\Delta H_i)$	$\frac{(-\Delta H_i)}{R} = \left(\frac{\partial \ln(P)}{\partial(1/T)}\right)_{q_i}$	-	[20]
Heat axial dispersion coefficient	λ_e	$\lambda_e = [7 + 0.5(Pr)(Re)]k_g$	-	[66]
Prandtl-Number	Pr	$Pr = \frac{\hat{C}_{pg}\mu}{k_g}$	$\hat{C}_{pg} = \frac{C_{pg}}{\sum_{i=1}^{NoC} y_i M_i}$ $C_{pg} = \sum_{i=1}^{NoC} y_i C_{pg,i}$	[65]
Reynolds Number	Re	$Re = \frac{\rho_g v d_p}{\mu_g}$	-	[65]
Gas Thermal Conductivity	k_g	$k_g = \sum_{i=1}^{NoC} \frac{y_i k_{g,i}}{\sum_{j=1}^{NoC} y_j \emptyset_{ij}}$	$k_{g,i} = \left(\hat{C}_{pg,i} + \frac{5}{4}\frac{R_g}{M_i}\right)\mu_i$	[65]
Heat transfer coefficient between the gas and the wall	h_w	$h_w = \frac{Nu k_g}{d_i}$	-	[65]
Overall Heat Transfer Coefficient	U_o	$\frac{1}{U_o} = \frac{1}{h_w} + \frac{e d_i}{k_w d_{ln}}$	$d_{ln} = \frac{(d_{ext} - d_i)}{\ln \frac{d_{ext}}{d_i}}$ $e = \frac{1}{2}(d_{ext} - d_i)$	[67]

Source: own authorship.

4.4.4. Momentum Parameters

Wilkes semiempirical equation was employed to estimate the mixture viscosity. In Table 6, the dimensionless parameter $\emptyset_{ij}$ depends on the pure gas viscosities (μ_i or μ_j) at system temperature and pressure (calculated by the aid of Lennard Jones parameters as detailed in Bird *et al.*(2007)) and the molar mass of species *i* or *j* (M_i or M_j). Since $\emptyset_{ij}$ is a binary parameter, its value must be calculated for all the different binary combinations of the ternary mixture. The gas mixture density is calculated from the ideal gas law.

Table 6. Momentum parameters.

Parameter	Symbol	Equation	Auxiliary equation	Reference
Viscosity	μ_g	$\mu_g = \sum_{i=1}^{NoC} \frac{y_i \mu_j}{\sum_{j=1}^{NoC} y_j \emptyset_{ij}}$	$\emptyset_{ij} = \frac{1}{8}\left(1+\frac{M_i}{M_j}\right)^{-1/2}\left[1+\left(\frac{\mu_i}{\mu_j}\right)^{1/2}\left(\frac{M_i}{M_j}\right)^{1/2}\right]$	[65]
Density	ρ_g	$\rho_g = \frac{P \sum_{i=1}^{NoC} M_i y_i}{R_g T_g}$ or $\rho_g = C_g\left[\sum_{i=1}^{NoC} M_i y_i\right]$	-	-

Source: own authorship.

4.5. Numerical method and software

The mathematical model was solved via gPROMS software (Process System Enterprise, UK). The discretization algorithm employed is the centered finite difference method (CFDM) of second order with 94 discretization intervals.

5. RESULTS AND DISCUSSION

5.1. Adsorbent textural properties

The N_2 adsorption/desorption isotherm on zeolite 13X at -196 °C is shown in Figure 18. The isotherm type can be classified as reversible type I (a) according to IUPAC classification [21]. No hysteresis loop is observed, as expected, in a predominantly microporous material and micropore filling is observed specially at low coverage where the adsorbed amount increases abruptly. The isotherm shape also exhibits concavity to P/P_0 axis and a limiting value for the adsorbed amount [21].

Figure 18. N_2 adsorption/desorption isotherm on zeolite 13X at -196 °C.

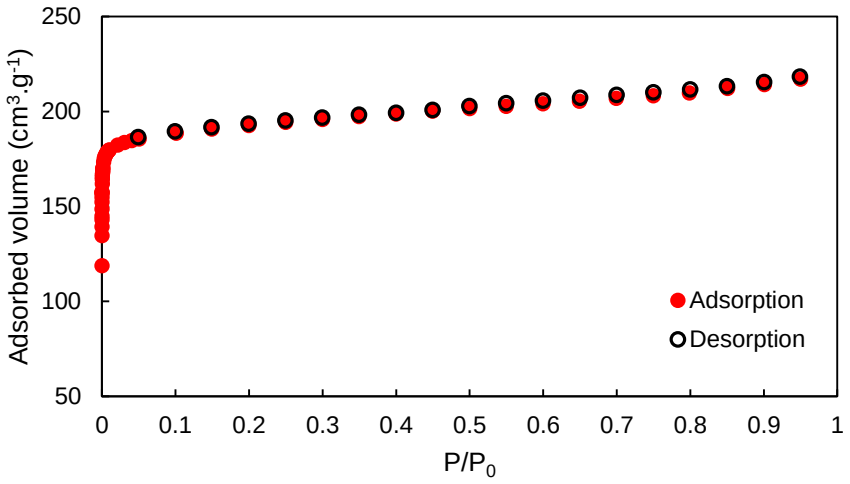

Source: Own authorship

The textural properties of zeolite 13X obtained from N_2 adsorption/desorption isotherm are summarized on Table 7. The BET surface area was estimated following Rouquerol *et al*. (2014) recommendations. In our case, the BET equation was applied to a relative pressure range between 0.002 and 0.010 (i.e., $0.002<P/P_o<0.010$).

The total pore volume was estimated at a relative pressure (P/P_0) equals to 0.95. Higher relative pressure values than selected one were omitted to avoid bias in case of condensation occurrence taking into consideration that the adsorbate is close to saturation pressure.

Table 7. Textural properties of the adsorbent

Textural characteristics	**Zeolite 13X**
BET surface area (m^2g^{-1})	806
Micropore volume (cm^3g^{-1})	0.29
Total pore volume (cm^3g^{-1})	0.34
Microporosity (%)	86

Source: Own authorship

The BET surface area value is in accordance with values of 710 m^2g^{-1} [68] and 743 m^2g^{-1} [69] found in literature.

5.2. Gas pure and binary isotherms for CO_2 and N_2

Pure CO_2 and N_2 isotherms on zeolite 13X were initially performed at 50 °C (Figure 19) in order to simulate post-combustion scenario. The experimental data shows that the adsorbent exhibits a much higher selectivity for CO_2 over N_2 in a reasonably wide range of pressure (0-10 bar). This fact also confirms the predominance of the equilibrium mechanism in the separation of CO_2 from N_2 on zeolite 13X under the studied conditions. The superior adsorption capacity of CO_2 can be explained as well by the difference in the critical temperatures of CO_2 (31.3 °C) and N_2 (-146.9 °C), i.e., CO_2 displays a condensable vapor like behavior that makes it more "adsorbable" whereas N_2 behaves as a supercritical gas [70].

Figure 19. Pure CO_2 and N_2 experimental adsorption isotherms at 50 °C on zeolite 13X.

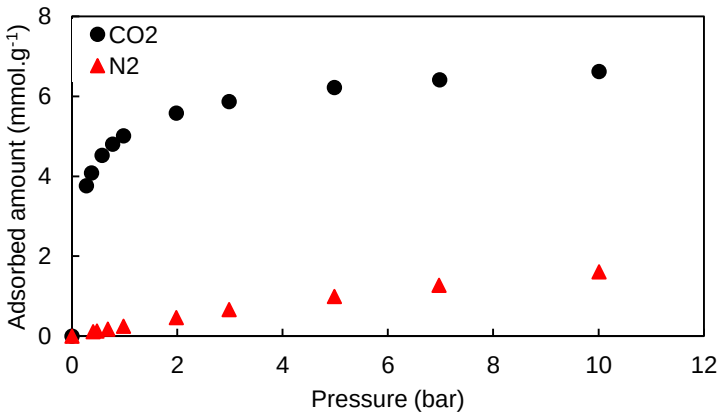

Source: Own authorship

CO_2 single isotherm exhibits a steep uptake at low pressure levels probably because of the enhanced adsorbent-adsorptive interactions in narrow micropores at the beginning of the micropore filling process [21] whereas pure experimental N_2 isotherm displays a straight line like behavior. The pure CO_2 and N_2 experimental isotherms were also obtained at other two temperatures, one over (75 °C) and one below (25 °C) the original temperature respectively, in order to establish temperature dependency of equilibrium isotherms to be further used in simulation process.

Among the various isotherm equilibrium models available in the literature, Sips model was originally employed to fit the experimental isotherm data due to its accuracy and feasibility to be extended in multicomponent mixtures. Sips model fittings, for CO_2 and N_2 single isotherms (Figure 20) for the three selected temperatures (25, 50 and 75°C), showed good agreement with experimental data for the two gases. Experimental data confirms, as expected, physical adsorption occurring for both isotherms since increasing the temperature results in an adsorption capacity drop and vice versa.

Figure 20. CO_2 (black) and N_2 (red) pure adsorption isotherms at 25 °C (circle), 50 °C (square) and 75 °C (triangle) on zeolite 13X. Symbols for experimental data and dashed line represents Sips model fitting.

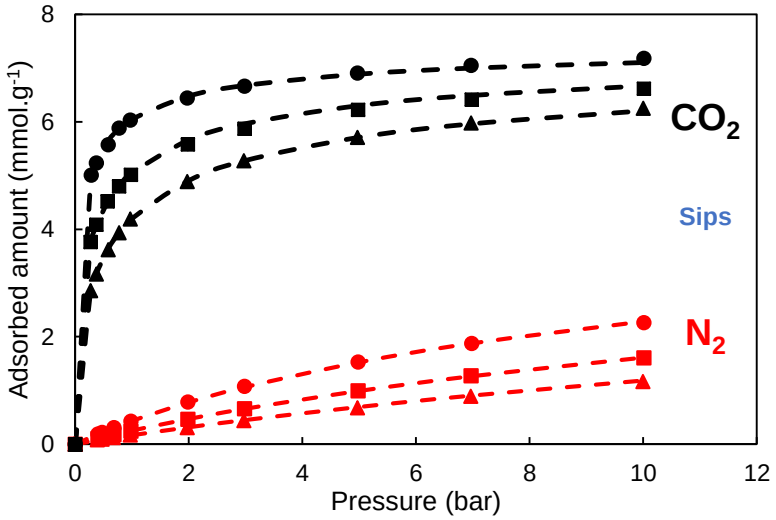

Source: Own authorship

Considering Sips model thermodynamic inconsistency at low coverage, isotherm data was also fitted to Toth equation (Figure 21), which exhibited good agreement at both low and high coverage and reduces to Henry Law at low-pressure levels. The Toth model disadvantage is the impossibility to be extended for multicomponent systems. Nonetheless, for this case, single model fitting works well for CO_2-N_2 binary system, due to the high selectivity the solid showed to adsorb CO_2 during dynamic tests, as will be further demonstrated in the breakthrough experiment section.

Figure 21. CO_2 (black) and N_2 (red) pure adsorption isotherms at 25 °C (circle), 50 °C (square) and 75 °C (triangle) on zeolite 13X. Symbols for experimental data and solid line represents Toth model fitting.

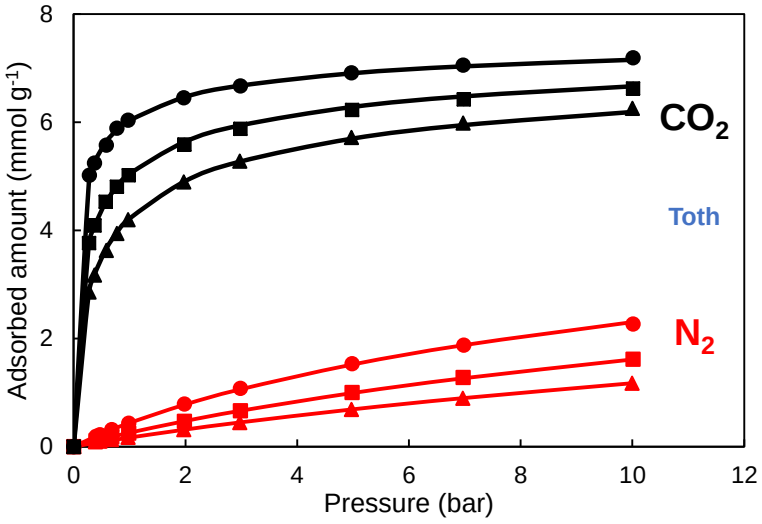

Source: Own authorship

The fitting parameters of Sips and Toth models for single adsorption isotherms of CO_2 and N_2 are shown in Table 8.

The q_{max} and n parameters were kept constant over the whole temperature range while the affinity parameter (b) was considered dependent of the temperature in both models as specified below:

$$b = b_0 \times exp\left(\frac{Q_0}{R_g T}\right) \quad (54)$$

where Q_0 represents a measure of adsorption heat [71] and R_g is the ideal gas constant. The equation (54) was linearized and plotted varying the temperature to calculate b_o and Q_0 values. The linearity correlation coefficient (R^2) was also computed and its values for each isotherm model fitting are listed in Table 2.

Table 8. Fitting parameters of Sips and Toth models for pure adsorption isotherms of CO_2 and N_2 on zeolite 13X in the temperature range 25–75 °C for 0–10 bar.

	Sips		**Toth**	
Parameter	CO_2	N_2	CO_2	N_2
q_{max} **(mmol g^{-1})**	7.620	4.895	7.911	6.604
b_o **(bar^{-1})**	5.72E-06	5.18E-05	5.01E-05	4.67E-05
n	1.815	1.0518	0.445	0.732
Q_0 **(J mol^{-1})**	-3.59E+04	-1.84E+04	-3.59E+04	-1.85E+04
R^2	0.996	0.998	0.996	0.999

Source: Own authorship

All of the parameters of the isotherm fittings were estimated by iterations minimizing the error between the fitted and the experimental data including linearization of equation (1) (i.e., minimizing (1- R^2)). In order to assess the accuracy of the two model fittings regarding the experimental data, the average relative error (*ARE*) was estimated. The values of *ARE* are presented in Table 9 and were obtained by the following equation:

$$ARE = \frac{100}{m}\sum_{i=1}^{m}\left|\frac{y_{exp} - y_{cal}}{y_{exp}}\right| \tag{55}$$

where y_{exp} refers to one point in the experimental isotherm, y_{cal} refers to the same point in the isotherm but from the model fitting and m is the number of data.

Both models displayed alike average relative errors with no drastic difference neither for each of the three isotherm temperatures nor for the two adsorbates. This result is in accordance with the model fittings in Figure 20 and 21 where both models have a similar behavior.

Table 9. Average Relative Error (ARE) for Sips and Toth model on adsorption experimental data fitting.

Temperature		Sips	Toth
		ARE (%)	ARE (%)
25 °C	**CO_2**	0.45	0.33
	N_2	0.90	1.09
50 °C	**CO_2**	0.75	0.56
	N_2	0.53	0.62
75 °C	**CO_2**	0.19	0.38
	N_2	4.94	5.33

Source: Own authorship

Binary adsorption isotherm for CO_2 and N_2 (15/85 % v/v) was performed at 50 °C and fitted to Extended Sips model as seen in Figure 22. Extended Sips model simply employs single isotherm fitting parameters and applies them into an extended equation taking into account both gases adsorption capacities at a certain temperature and their partial pressure in the mixture. Although the adjustment exhibited fair agreement with experimental data, a slightly underestimation bias is always noticeable for all the experimental data in the pressure range under study. This behavior was reflected in the ARE value (3.15 %) on the fitted isotherm, which was higher in comparison with the ARE values obtained in the pure isotherm models at 50 °C. The fitting parameters of Extended Sips model for the binary mixture are presented in Table 10.

Figure 22. Binary adsorption isotherm for CO_2-N_2 (15/85 % in molar basis) at 50 °C on zeolite 13X. Symbols represent experimental data and solid line represents Extended Sips model fitting.

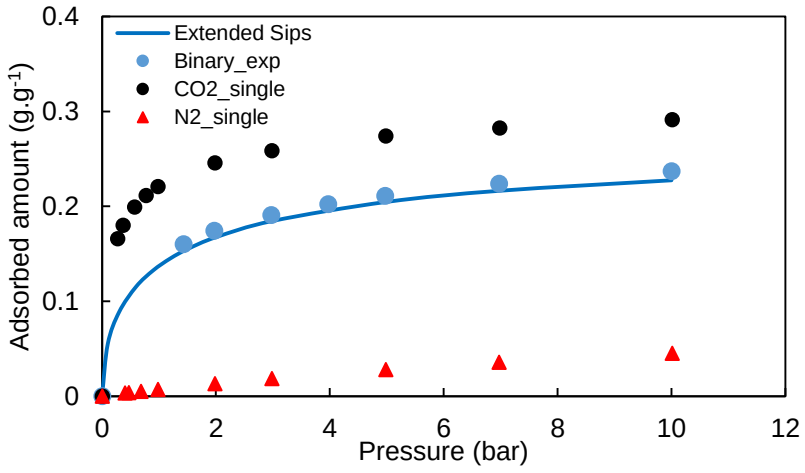

Source: Own authorship

Table 10. Fitting parameters of Extended Sips model for CO_2 and N_2 (15/85 % v/v) binary isotherm at 50 °C

Parameter	**CO_2**	**N_2**
y_i	0.15	0.85
q_{max} (gg^{-1})	0.335	0.137
b (bar^{-1})	3.423	0.047
n	1.815	1.052

Source: own authorship

5.3. Breakthrough experiments and simulations

A CO_2 (15 % v/v) breakthrough diluted in Helium at 50 °C and 1 bar was initially performed three times to check repeatability of the FBU. The test results showed good precision as exhibited in Figure 23, once all runs displayed the same trend.

Figure 23. Repeatability test: CO_2 (15 % v/v) breakthrough at 50 °C.

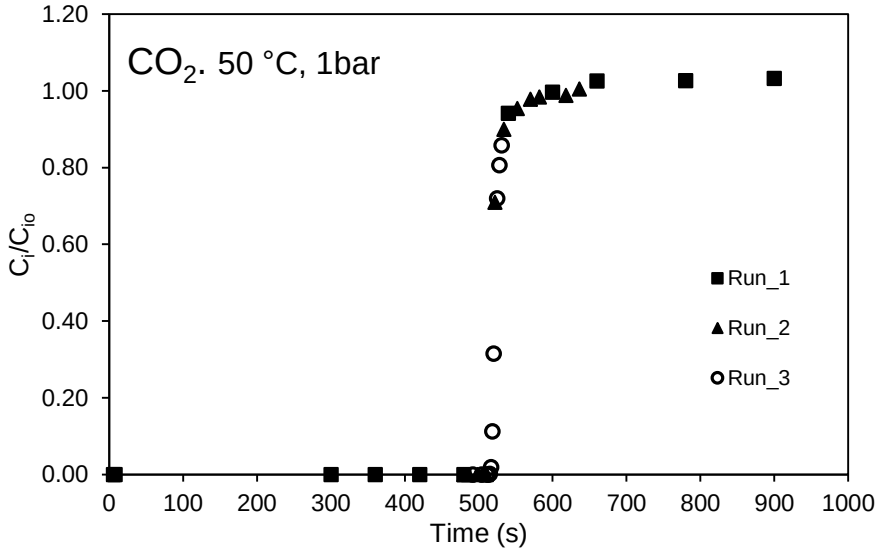

Source: own authorship

This test was also carried out for CO_2 at the same composition at 25 and 75 °C. The fixed bed adsorption capacities derived from breakthrough data at these three temperatures represent the amount of CO_2 adsorbed in equilibrium with the adsorbate pressure (i.e., P=0.15 bar). These adsorption capacities were later compared to their respective equilibrium isotherms to verify breakthrough test reproducibility. Despite the fact that these tests were completed employing

different equipment, methodology and uncertainty, one can expect breakthrough data to be in fair agreement with equilibrium data. In Figure 24, one can see that the fixed bed adsorption capacities (dynamic test) match the experimental equilibrium isotherm data (static test), which guarantees the accuracy of the results.

Figure 24. Comparison between static and dynamic tests for reproducibility. Black symbols represent isotherm experimental data; red symbols represent fixed bed adsorption capacity from breakthroughs.

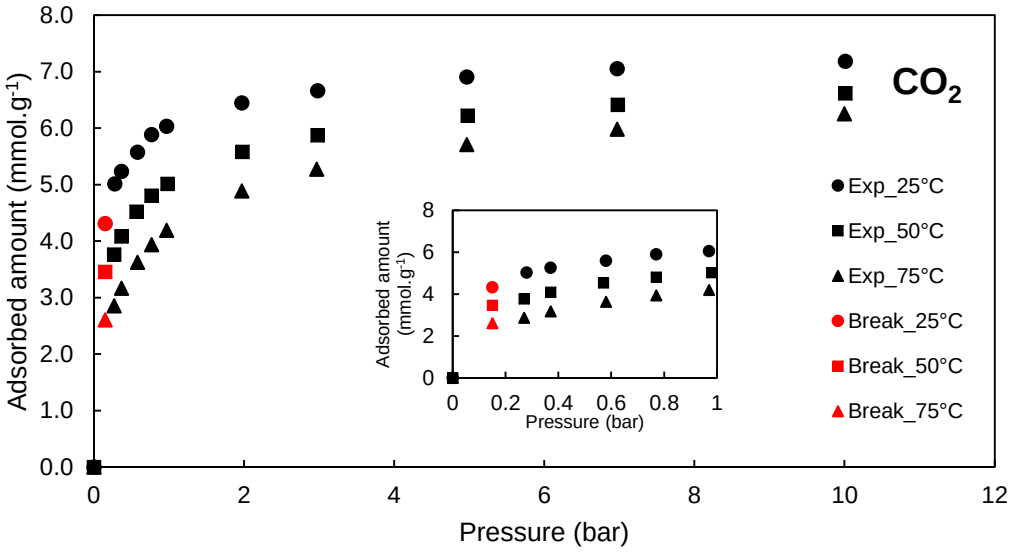

Source: own authorship

Experimental breakthrough curves for binary mixture CO_2-N_2 (15/75 % v/v) in He (10 % v/v) at three different temperatures (25, 50 and 75 °C) are displayed in Figure 25. As expected in physical adsorption, increase in temperature decreases adsorption capacity and thus separation performance. For all the three temperatures under study, a very quick breakthrough point for N_2 was observed suggesting meaningful separation between CO_2 and N_2. Additionally, N_2 exhibited a deeply steep Mass Transfer Zone (MTZ) indicating hardly any mass transfer resistance during adsorption step. In contrast, CO_2 presented a more dispersive MTZ denoting the existence of mass transfer resistances. All the breakthrough curves in Figure 25 displayed typical behavior of multicomponent breakthrough curves since the weakly adsorbed component (N_2) experienced the so-called roll-up effect due to the continuous displacement of N_2 caused by the propagation of CO_2 front along the fixed bed.

Figure 25. Experimental breakthrough curve for CO_2-N_2 (15/75 % v/v) in He (10 % v/v) at 25, 50 and 75 °C on zeolite 13X.

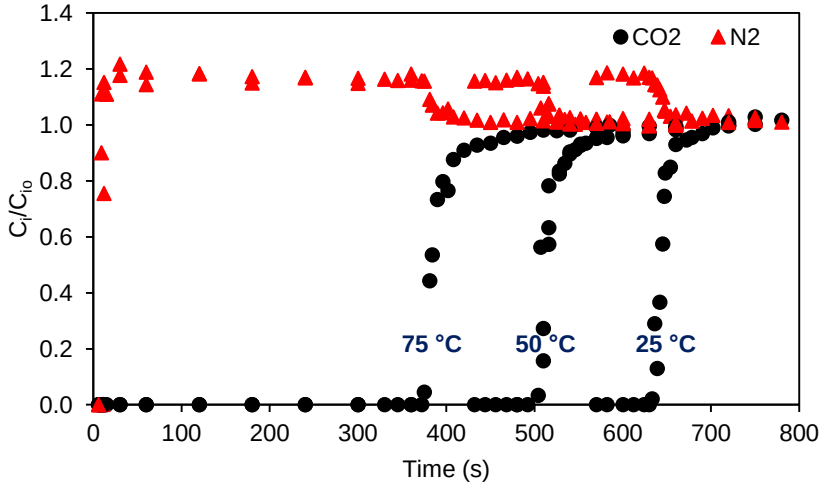

Source: own authorship

The CO_2 adsorbed amount and the fixed bed adsorption capacities, derived from the aforementioned breakthrough curves, are listed in Table 11.

Table 11. Fixed bed adsorption capacity for CO_2.

Temperature	**CO_2 retained amount (mmol)**	**CO_2 fluid amount (mmol)**	**CO_2 adsorbed amount (mmol)**	**Fixed bed adsorption capacity (mmol $CO_2.g^{-1}$)**
25 °C	5.644	0.004	5.64	4.3
50 °C	4.532	0.002	4.53	3.5
75 °C	3.413	0.003	3.41	2.6

Source: own authorship.

As shown above in Table 11, the amount of CO_2 in fluid phase in the fixed bed is negligible in comparison with the amount retained. Most of the CO_2 is practically retained in adsorbed phase within the column once the working pressure is close to atmospheric pressure. Moreover, it is worth mentioning that N_2 adsorption capacity was not included in Table 11 once breakthrough times were slightly negative or scarcely above zero when subtracting dead time for experiment conditions. This experimental behavior is owed to the very quick breakthrough time [54] and the large rolled-up area [72] exhibited by N_2 which confirms the large selectivity of zeolite 13X for CO_2 adsorption.

Some numerical errors regarding isotherm-fitting models arose when running breakthrough curve simulations once Sips and Toth models exhibited roots of negative numbers in their equations during the iteration routine respectively. In order to overcome this problem, a mathematical arrangement that converted the negative value in zero was included within the program code. Although it worked well for Toth model (not so for Sips model), the iteration routine became very slow. That said, a different isotherm model was therefore employed to complete the simulations and avoid the arising numerical errors. A version of Dual-Site Langmuir (DSL) isotherm, which was found to provide good results in simulations [48, 73] was selected:

$$q_{e_i} = \frac{IP_{1i} \times exp\left(\frac{IP_{2i}}{T}\right) \times P_i}{1 + IP_{3i} \times exp\left(\frac{IP_{4i}}{T}\right) \times P_i} + \frac{IP_{5i} \times exp\left(\frac{IP_{6i}}{T}\right) \times P_i}{1 + IP_{7i} \times exp\left(\frac{IP_{8i}}{T}\right) \times P_i} \quad (56)$$

where IP_{1i}, IP_{2i}, ..., IP_{8i} are the isotherm model parameters of the component i.

The fitted pure CO_2 and N_2 adsorption isotherms by this version of DSL model presented good agreement with experimental data as one can see in Figure 29. The isotherm model parameters are listed in Table 12.

Figure 26. CO_2 (black) and N_2 (red) pure adsorption isotherms at 25 °C (circle), 50 °C (square) and 75 °C (triangle) on zeolite 13X. Symbols are experimental data and round dots represent DSL model fitting.

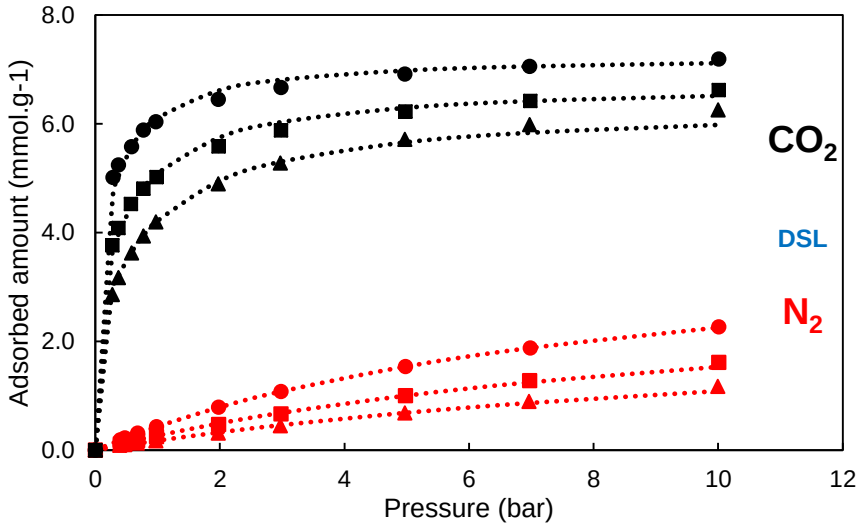

Source: own authorship.

Table 12. Fitting parameters of DSL model for pure adsorption isotherms of CO_2 and N_2 on zeolite 13X in the temperature range 25–75 °C for 0–10 bar.

CO_2							
IP1	**IP2**	**IP3**	**IP4**	**IP5**	**IP6**	**IP7**	**IP8**
mmol $g^{-1}.bar^{-1}$	K	bar^{-1}	K	mmol $g^{-1}.bar^{-1}$	K	bar^{-1}	K
9.79E-05	7290.089	1.09E-04	7015.92	2.00E-03	2694.486	1.01E-03	2419.54
N_2							
IP1	**IP2**	**IP3**	**IP4**	**IP5**	**IP6**	**IP7**	**IP8**
mmol $g^{-1}.bar^{-1}$	K	bar^{-1}	K	mmol $g^{-1}.bar^{-1}$	K	bar^{-1}	K
1.78E-04	7290.089	1.14E-04	7015.92	6.42E-04	2694.486	4.45E-03	2419.54

Source: own authorship.

The breakthrough curve simulations for CO_2 -N_2 (15/75 % v/v) in He (10 % v/v) at 25, 50 and 75 °C are presented in Figures 26-28. For all the breakthrough curves, a total volumetric flowrate value of 80 cm^3min^{-1} STP was used.

Figure 27. Breakthrough curve for CO_2 -N_2 (15/75 % v/v) in He (10 % v/v) at 25 °C. 1bar. Symbols represent experimental data; lines and dashed lines represent simulated data.

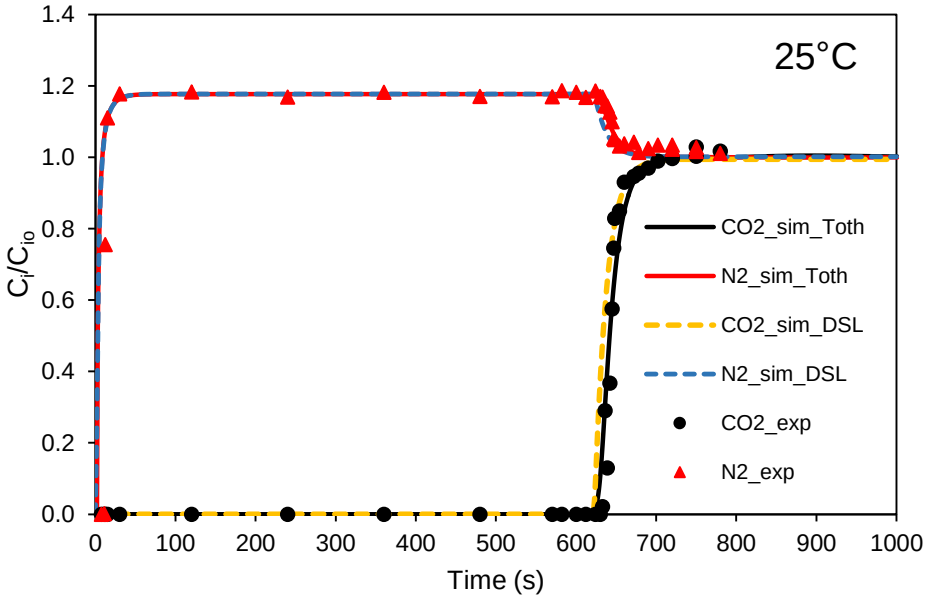

Source: own authorship

Figure 28. Breakthrough curve for CO_2 -N_2 (15/75 % v/v) in He (10 % v/v) at 50 °C. 1bar. Symbols represent experimental data; lines and dashed lines represent simulated data.

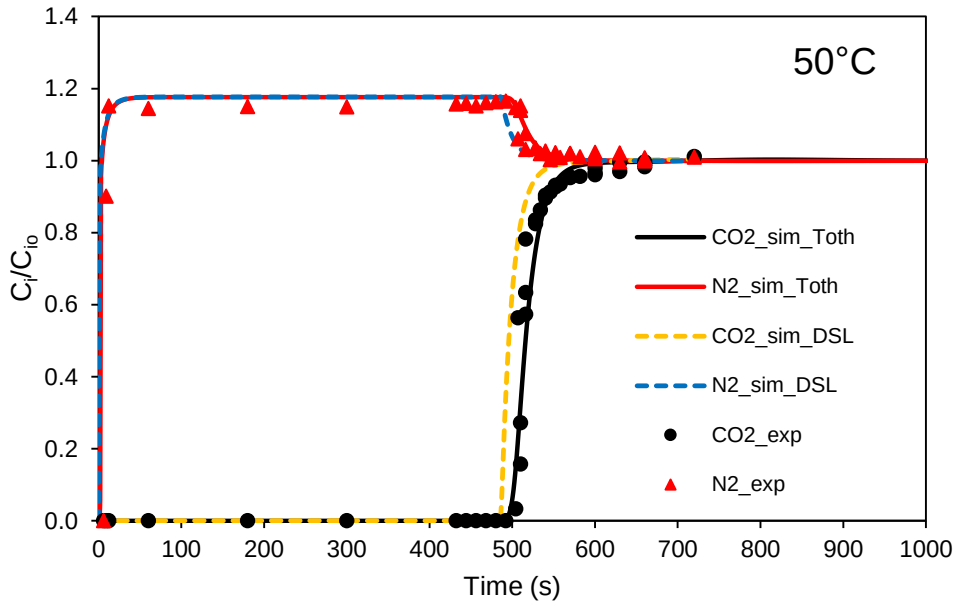

Source: own authorship

Figure 29. Breakthrough curve for CO_2 -N_2 (15/75 % v/v) in He (10 % v/v) at 75 °C. 1bar. Symbols represent experimental data; lines and dashed lines represent simulated data.

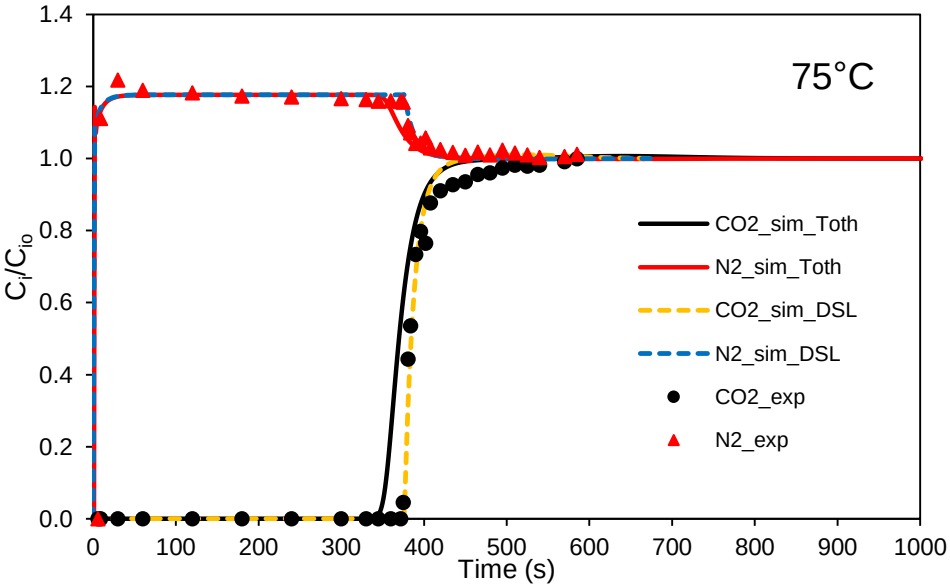

Source: own authorship

The proposed mathematical model matched well the experimental breakthrough data overall. A closer look at Figures 27-28 evidence minimal mismatches when using DSL isotherm model for breakthrough simulations at 50 °C and Toth isotherm model for breakthrough simulations at 75 °C. Once all the proposed model parameters are the same regardless the isotherm model employed in the simulations, one could suppose that the difference between experimental and simulated data relies on the isotherm model fittings for each temperature. In order to prove the abovementioned, a comparison between the fixed bed capacities for CO_2 and the equilibrium adsorbed amount from isotherm model fittings at 50 °C and 75 °C for CO_2 at 0.15 bar is established in Table 13.

Table 13. Comparison between fixed bed adsorption capacity and amount adsorbed for CO_2 in Toth and DSL isotherm model.

Temperature	**50 °C**	**75 °C**
Experimental Breakthrough (mmol CO_2 g^{-1})	3.5	2.6
Toth model (mmol CO_2 g^{-1})	3.1	2.3
DSL model (mmol CO_2 g^{-1})	3.1	2.6

Source: own authorship

For the case of 75 °C, the foregoing assumption appears to be valid since DSL model matches experimental breakthrough data and Toth model underestimate fixed bed adsorption capacity. On the contrary, for 50 °C, despite both isotherm models exhibit the same underestimated adsorption capacity, unexpectedly Toth model manages to fit well the experimental breakthrough data.

The issue of whether to use a non-multicomponent extended isotherm model for simulation of binary breakthroughs was also evaluated for CO_2-N_2 separation by zeolite 13X under this study conditions. A comparison of the fixed bed capacity values for CO_2 at 50 °C for single and binary breakthrough shows that they are practically the same (3.49 mmol. g^{-1} vs. 3.46 mmol. g^{-1} respectively), confirming the feasibility of employing single component isotherm models for CO_2-N_2 binary system. The same conclusion on this matter had already been reported in the literature [54] where single component adsorption equilibrium by Toth model was successfully used for prediction of CO_2-N_2 binary breakthrough curves. For the cases in which single and binary

data do not reproduce, the IAST prediction for multicomponent mixtures may be applied as reported elsewhere [55].

For all the simulations, the mass transport coefficient K_{LDF} was fitted to the experimental breakthrough curves. A K_{LDF} value of 0.10 s^{-1} was found to be suitable for the experimental breakthrough data in the range of 25-75 °C for both CO_2 and N_2. The K_{LDF} value influences in the size and the steepness of the Mass Transfer Zone (MTZ) as one can appreciate in Figure 31. A lower value of K_{LDF} implies slower kinetics increasing the size of the MTZ. A higher value of K_{LDF} makes the separation process more efficient once the rate of mass transport is enhanced making the MTZ steeper (i.e., more ideal) and correspondingly reducing the length of unused bed.

Additionally, it is worth noting that the stoichiometric time (t_{st}) is unaffected by the mass transport coefficient once the t_{st} value remains identical regardless the size of the MTZ as seen in Figure 30. In either case, the t_{st} value is directly related to the fixed bed adsorption capacity and not to the MTZ dispersion.

Figure 30. Mass transport coefficient (K_{LDF}) sensibility for breakthrough experiments.

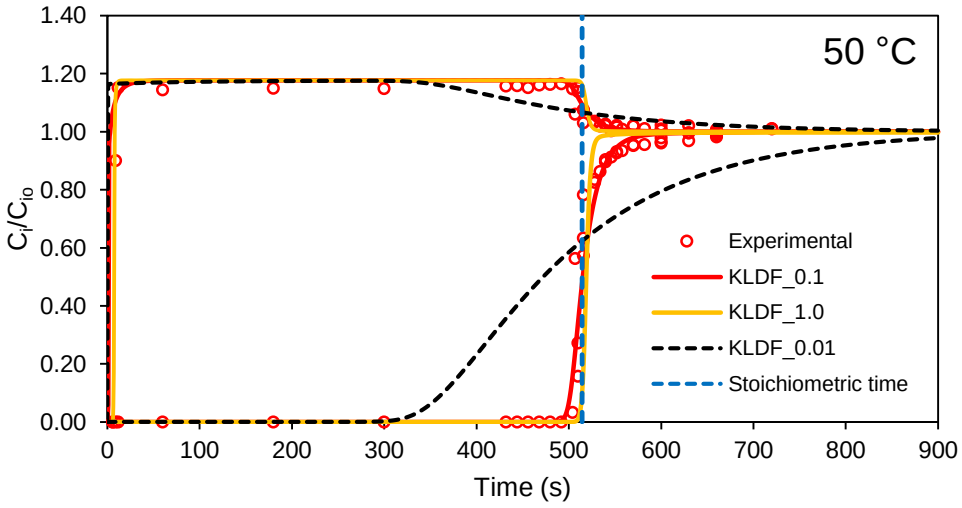

Source: own authorship

Thermal effects are key in large-scale separation by adsorption once separation efficiency may be affected by the increase in the design temperature during adsorption step. The heat of adsorption is the main responsible for that heat generation, nevertheless several other factors

may influence the heat confinement within the column such as a poor adsorbent thermal conductivity or a low overall heat transfer coefficient between the gas and the wall.

Figure 31. (a)Adiabatic and non-adiabatic breakthrough curve for CO_2-N_2 (15/75 % v/v) in He (10 % v/v) at 50 °C. (b) Gas temperature (Tg) and wall temperature (Tw) profile at the column exit for adiabatic and non-adiabatic conditions.

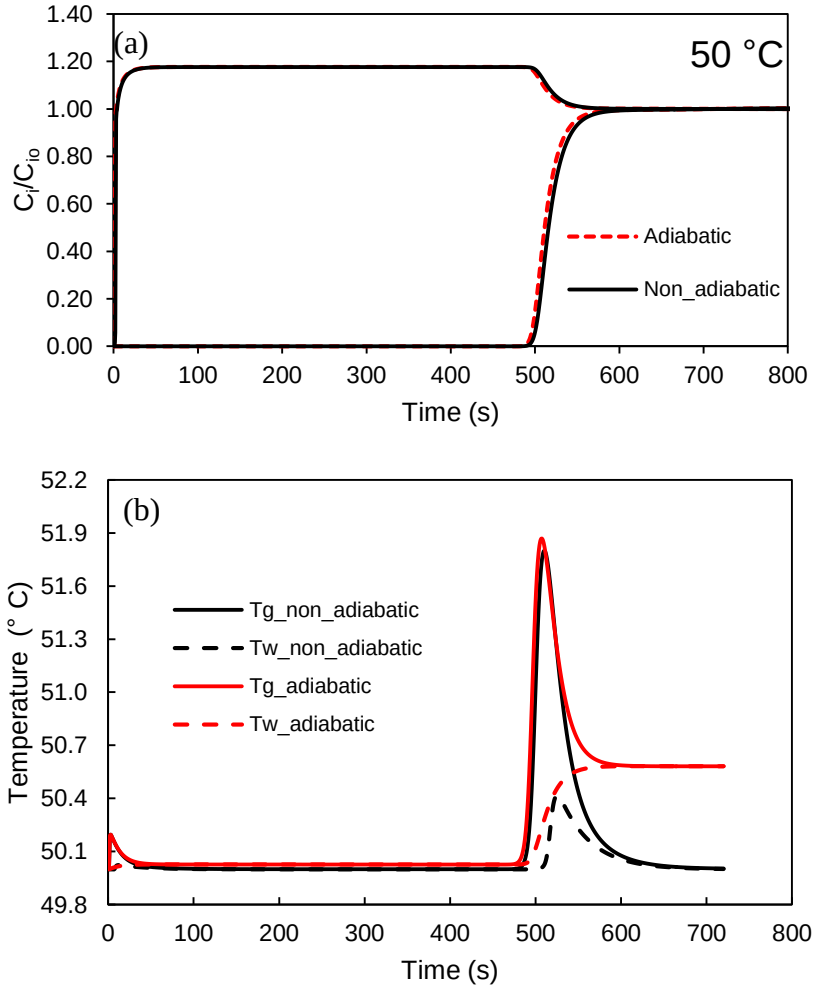

Source: own authorship

If heat exchange between the system and the environment is not fast enough, the system temperature will indisputably increase by the heat accumulation within the bed. The proposed model is conceived to simulate a non-adiabatic system. Even though our experimental rig was unable to register the gas temperature *in situ*, the proposed mathematical model was indeed capable to predict the gas and the wall temperature behavior with time at any axial position. For that reason,

a temperature profile comparison between an adiabatic (U_0=0) and non-adiabatic system was developed to unveil the eventual impact on the breakthrough prediction provided that an adiabatic system was assumed. As can be observed in Figure 31 (a), the adiabatic system assumption for this case does not fail to predict the breakthrough dynamics once the two curves practically overlapped.

In Figure 31 (b), the temperature profiles for the adiabatic and non-adiabatic system at the end of the column are presented. Two peaks of different size are prominent for both gas temperature profiles, corresponding to the N_2 and CO_2 breakthrough points respectively. The wall temperature appears not be affected by N_2 adsorption front at breakpoint once N_2 heat of adsorption is not high enough to cause wall temperature increase. The contrary occurs at CO_2 breakpoint. For the adiabatic system, the gas and the wall temperature at the column exit, by the time the bed is saturated, do not recover the feed value once there is no existence of heat exchange with the surroundings. On the other hand, for the non-adiabatic conditions, the gas and the wall temperature are able to attain the feed value when thermal equilibrium with the environment is achieved.

Albeit the adiabatic assumption may be applied under these study experimental conditions, it cannot be extended to large-scale systems without further validation once thermal effects are not appreciable in this study conditions given the small laboratory scale of our experiments. In either of the cases previously discussed, the gas temperature increase is no more than 2 °C, a very small value to consider a significant influence in breakthrough prediction due to thermal effects.

The model parameters employed for all breakthrough simulation runs were obtained, measured or estimated according to section 4.4. The physical properties of the adsorbent and the fixed bed are specified in Table 14 and 15 respectively.

Table 14. Physical Properties of the adsorbent

Particle size	-	-600+425	μm
Solid density	ρ_s	2398	Kg m^{-3}
Particle density	ρ_p	1195	Kg m^{-3}
Particle porosity	ε_p	0.45	-
Particle diameter	d_p	5.12E-4	m
Solid specific heat	$\hat{C}_{ps}$	920	J Kg^{-1} K^{-1}
Specific solid volume	$\hat{V}_s$	44.17E-05	m^3 Kg^{-1}
Specific pore volume	$\hat{V}_p$	36.49E-05	m^3 Kg^{-1}

Source: own authorship

Table 15. Physical Properties of the fixed bed.

Bed length	L_o	0.1	m
Bed mass	m_{ads}	1.3E-03	Kg
Bed density	ρ_b	943.7	Kg m^{-3}
Internal column diameter	d_i	4.2E-03	m
External column diameter	d_{ext}	4.6E-03	m
Bed porosity	ε	0.24	-
Column wall specific heat	$\hat{C}_{pw}$	477	J $Kg^{-1}K^{-1}$
Column wall density	ρ_w	7860	Kg m^{-3}

Source: own authorship

Some model parameters were related to gas temperature by the aid of an equation obtained by linear regression. The model parameters were adjusted in a temperature range between 25 and 300 °C since they were also used for desorption simulations. In fact, the idea of correlating some parameters to temperature changes is owed principally to the temperature swing during desorption step. However, as already addressed in the simulated gas temperature discussion, despite breakthrough experiments are intended to be performed at constant temperature, some fluctuations are perceived mainly due to heat of adsorption generated. The parameters and the equations describing the temperature dependence are shown in Table 16. These parameters were chosen given their higher sensibility to temperature fluctuations. Model parameters different from those listed in Table 16 were kept constant for a specific breakthrough temperature. In addition, it is worth to note that the linear correlation coefficient showed good adjustment for all the equations in the temperature range selected.

Table 16. Some model parameters temperature dependence between 25 and 300 °C.

Parameter	**Equation***	**R^2**
Gas mixture Viscosity *(μ_g)* [$Kg.m^{-1}s^{-1}$]	$\mu = 4E-08 * T_g + 6E-06$	0.998
Axial mass dispersion *(D_{ax})* [m^2s^{-1}]	$D_{ax} = 9E-08 * T_g - 8E-06$	0.997
Mixture Conductivity (K_g) [$Wm^{-1}K^{-1}$]	$k_g = 7E-05 * T_g + 0.0083$	0.999
Heat transfer coefficient between gas and wall (h_w) [$Wm^{-2}K^{-1}$]	$h_w = 2.672 * T_g + 1752.9$	1.000

* Gas Temperature (T_g) input is in Kelvin (K).

Source: own authorship

5.4. Desorption experiments and simulations

The desorption process efficacy has been assessed in terms of the CO_2 recovery in regard to the amount of CO_2 captured during the preceding adsorption step at 50 °C. Two desorption configurations for TSA as regeneration strategy were tested: *i*) *configuration 1*: regeneration by He purge and then temperature swing along with He purge and *ii*) *configuration 2*: regeneration by temperature swing along with He purge. For the former TSA configuration, the effect of decreasing the CO_2 partial pressure (purge) and the effect of heating could be evaluated separately, specifically the amount of CO_2 desorbed in each step. The relative concentration profile for the whole adsorption-desorption process for *configuration 1* is displayed in Figure 32.

Figure 32. Adsorption-desorption (*configuration 1*) process for CO_2-N_2 separation.

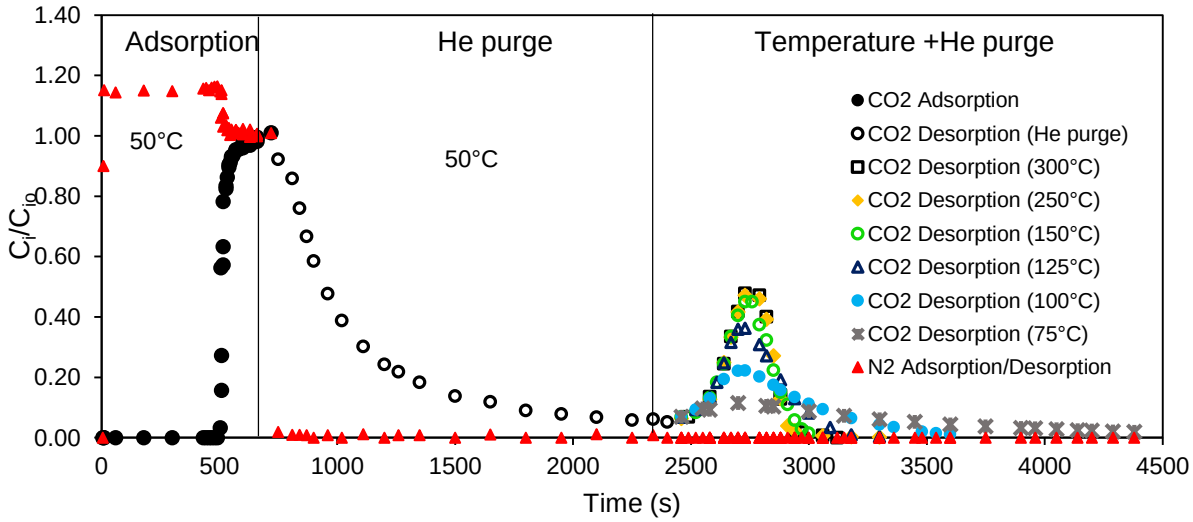

Source: own authorship

At first, one can observe the breakthrough curve for CO_2-N_2 at 50 °C in conditions previously discussed. Once bed saturation is attained (ca 720 s), the CO_2 and N_2 supply is stopped and the He purge is initiated, namely the He flowrate is increased 10 times, passing from 8 cm^3min^{-1} in the adsorption step to 80 cm^3min^{-1} STP to keep the total volumetric flow in the same value. On the one hand, the CO_2 relative concentration profile starts to decrease monotonically once its partial pressure is being decreased by the He flow passing continuously through the fixed bed. On the other hand, the N_2 relative concentration profile falls severely since N_2 was adsorbed in tiny

amounts. The Helium purge is ended as soon as the TCD sensor detects the minimal concentration of CO_2. Once recovery of CO_2 is not fully accomplished by purging, the system temperature is then increased (at 2400 s) using a 20 °C.min^{-1} ramp keeping the same He flowrate. Several CO_2 desorption profiles for different temperatures are shown in Figure 33. The first temperature selected for the heating stage was the adsorbent outgassing temperature employed in this study, i.e., 300 °C. Afterwards, subsequent lower values of temperatures were tested to investigate the influence of this parameter in CO_2 recovery. The relative concentration profile for the heating phase exhibits a maximum value, which increases with the regeneration temperature, while the end of the curves becomes lengthier when lowering the value of the regeneration temperature. This behavior can be explained by the fact that physisorption equilibrium is affected by increasing the temperature; consequently, CO_2 is desorbed more quickly.

The amounts of CO_2 desorbed by *configuration 1* are presented in Table 17. As one can see, the purging phase manages to desorb 77 % of the CO_2 earlier adsorbed. It is worth to clarify that full adsorbate recovery is generally accomplished in physisorption by means of inert purge for an infinite time; however, due to experimental limitation, the purging step is restricted to the TCD limit of detection. Furthermore, using an extended time for regeneration purposes would be impractical for industrial processes. Siriwardane *et al* (2005) evaluated a temperature programmed desorption on different zeolites for CO_2 capture in post-combustion scenario in a laboratory-scale fixed-bed reactor. For the case of zeolite 13X, they found similar results to those in this study: 62 % of the adsorbed amount of CO_2 was only possible to be recovered by means of N_2 purge and complete recovery was attained after applying a 120 °C regeneration temperature. They also suggested that there is a fraction of CO_2 weakly adsorbed and strongly adsorbed on zeolites. The former is the one desorbed by purge and the latter is the one recovered by heating.

Table 17. CO_2 recovery by *configuration 1*.

Adsorbed at 50 °C (saturation) (mmol CO_2)	**Desorbed from He purge (1) (mmol CO_2)**	**Desorbed from Temperature + He Purge (2) (mmol CO_2)**					
		300 °C	**250 °C**	**150 °C**	**125 °C**	**100 °C**	**75 °C**
4.53	3.49	1.09	1.08	1.03	1.09	1.05	1.01
% Recovery	*77%*	*24%*	*24%*	*23%*	*24%*	*23%*	*22%*
% Total recovery (1+2)	-	*101%*	*101%*	*100%*	*101%*	*100%*	*99%*

Source: own authorship.

A complete CO_2 recovery is achieved for *configuration 1* no matter the temperature used in the heating step as seen in Table 17. Total recovery values slightly over 100 % are considered to be within an experimental error of $\pm$ 1 %. However, the time to obtain full recovery varies with temperature as reported in Figure 33, with the exception of 250 °C, which exhibited the same behavior as 300 °C. This fact is meaningful once synchronization between adsorption and desorption steps is necessary for industrial processes, namely if one consider a separation process with two fixed beds: one bed is separating the mixture whereas the other one is being regenerated.

Figure 33. Time for adsorption and *configuration 1* regeneration strategy.

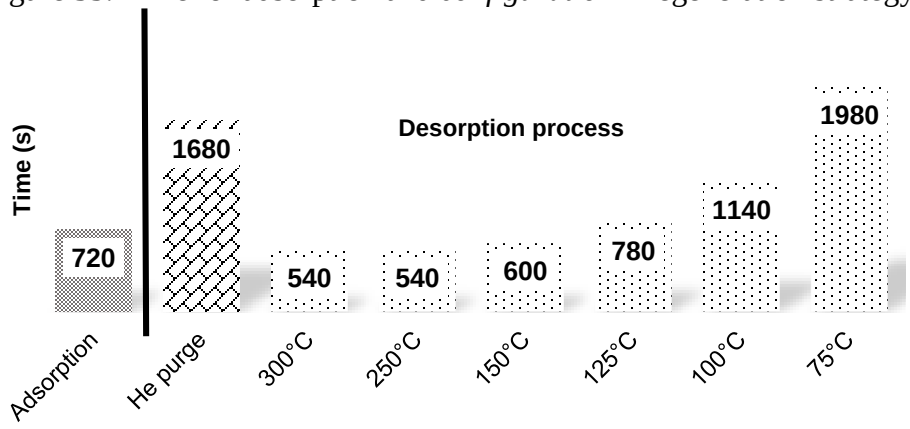

Source: own authorship.

For the case of *configuration 1*, only the He purge step duplicates the time taken for adsorption, which would be itself an inconvenient to make the system work continuously, once adsorption step would finish much earlier than desorption and thus, efficacy of CO_2 recovery would drop drastically if the cycle time is limited by the adsorption stage. In the same fashion, using an extended purge time would dilute considerably the CO_2 recovered which would affect the further storage and transport of this gas since larger equipment sizes would be necessary once total gas volume is increased.

In order to improve the lack of flexibility imposed by a two-bed TSA system, a third bed, called guard bed, has been suggested to be interposed in between the adsorber bed and the one in the regeneration phase [74]. By the time the adsorber is almost saturated, the beds are exchanged, i.e., the guard bed becomes the main adsorber, and the previous adsorber moves into the regeneration phase. The initial bed in regeneration stage becomes now the guard bed. By means of

this arrangement, the length of unused bed (LUB) is constantly restricted in the guard bed and the main adsorber is always saturated to almost its full capacity when the regeneration is about to initiate, consequently allowing a better use of the desorption energy. However, this scheme may not be profitable due to the additional cost generated by the third bed [74]. In any event, the number of additional beds for a suitable adsorption-desorption synchronization will rely on real desorption time (regeneration and cooling). In an adsorption process for CO_2 capture from flue gases, like this case, it is crucial to have small units to process uninterruptedly large volumes of feed [49]. Given these points, in this study, main discussion will be delimited to a two bed-TSA system.

The *configuration 2* is a way to merge the purging and heating step omitting the initial He purge, seeking a reduction in desorption time that enables synchronization with the adsorption phase. The relative concentration profile for the whole adsorption-desorption process for *configuration 2* can be seen in Figure 34. For this case, the number of temperatures tested was reduced to three, namely 300, 150 and 125 °C. The first temperature is maintained since it is the reference outgassing temperature for zeolite 13X used in this study. Once 100 and 75 °C took lengthy times in *configuration 1*, they have been skipped to be tested in *configuration 2*.

Figure 34. Adsorption- desorption (*configuration 2)* process for CO_2-N_2 separation.

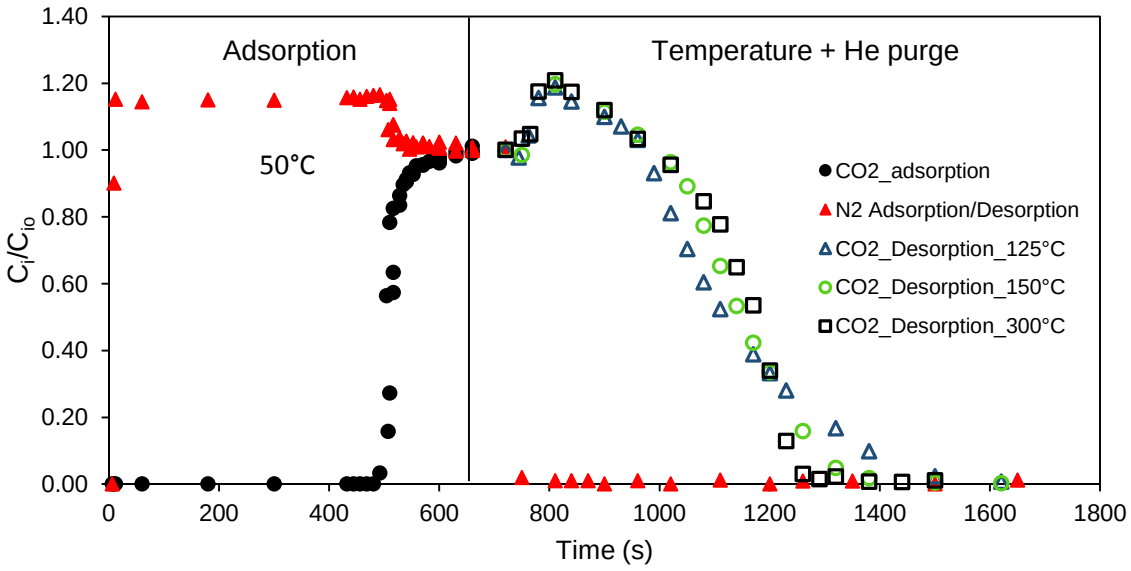

Source: own authorship

The CO_2 relative concentration profile, different from *configuration 1*, is not characterized by a monotonically decreasing function in this case. Instead, the curve exhibits a

maximum value, which for either of the cases, surpasses the initial CO_2 concentration. This fact is due to the impact that heating exerts on the CO_2 adsorbed molecules once when only purge was employed in *configuration 1*, this behavior was not observed. Clearly, the CO_2 adsorption is disadvantaged by thermodynamic equilibrium affectation via increasing the temperature. The amounts of CO_2 desorbed by *configuration 2* for the three temperatures tested are reported in Table 18.

Table 18. CO_2 recovery by *configuration 2*.

Adsorbed at 50°C (saturation) (mmol CO_2)	**Desorbed from Temperature + He Purge (mmol CO_2)**		
	300 °C	**150 °C**	**125 °C**
4.53	4.20	4.17	4.13
% Recovery	*93%*	*92%*	*91%*

Source: own authorship

The recovery amounts of CO_2 for each temperature tested are very alike, but none of them reached 100 % recovery as in *configuration 1*. In compensation, desorption time is enormously reduced by this regeneration configuration. Apart from that, for all the three regeneration temperatures tested, the desorption time is shorter than the adsorption time, which is convenient for a synchronization of the whole process. The desorption time increases again when lowering the regeneration temperature as seen in Figure 35.

Figure 35.Time for adsorption and *configuration 2* regeneration strategy.

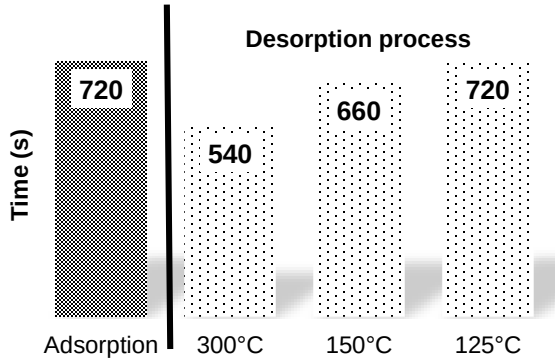

Source: own authorship

Given this points, some considerations must be taken into account to select a suitable regeneration configuration for CO_2 separation given the results obtained:

(1) The longer the desorption time, the more diluted the CO_2 concentration in the gas stream, so the larger the gas volume to be handled and thus the more expensive the storage and transport of CO_2.

(2) The higher the regeneration temperature, the higher the energy penalty and hence the more expensive the heating step.

In the light of the former consideration, *configuration 1* should be discarded given the infeasibility to be coupled with adsorption once desorption time is too long. In contrast, *configuration 2* would be appropriate if the adsorption phase limits the cycle time once either of the regeneration temperatures in *configuration 2* exhibited shorter desorption times. One may also think that according to the first consideration, a temperature of 300 °C would be the most suitable since it presented the shortest desorption time of all the assessed temperatures, however, in any event the adsorption time would be the reference time, consequently 150 and 125 °C may also be employed. According to the second consideration, the lowest temperature i.e., 125 °C would be the right choice because it would be the cheapest option. Nevertheless, in the final analysis, an economic evaluation would be necessary to find out the extent of cost saving upon selecting 125 °C as regeneration temperature for *configuration 2* in comparison with the two other temperatures tested. The truth is that a reduction in more than 50 % of the temperature value is accomplished when considering using 125 °C instead of 300 °C.

In order to introduce more tools to compare the regeneration temperatures tested in *configuration 2*, the values of the energy needed to heat the He purge gas stream to desorb the retained product in the fixed bed and the volume of purge gas employed during the desorption phase are presented in Table 19.

Table 19. Energy to heat He purge and He purge volume per mole of CO_2 desorbed in *configuration 2*

Temperature	**300 °C**	**150 °C**	**125 °C**
E_{He} **(KJ.mol^{-1} CO$_2$ desorbed)**	28.6	19.6	16.2
V_{He} **(m^3.mol^{-1} CO$_2$ desorbed)**	0.17	0.21	0.23

Source: own authorship.

As expected, the value of the energy required to heat the He purge per mole of CO_2 desorbed increases with the value of the regeneration temperature since more energy is employed to reach higher desorption temperature values. For the case of desorption at 300 °C, it is worth to clarify that the energy required for heating the purge gas stream was actually calculated for a temperature value of 230 °C, once regeneration was completed during the course of the temperature ramp. Despite that, since desorption was intended to be performed at 300 °C, the experiment reference is maintained at 300 °C. On the other hand, the purge volume amount decreases with higher values of the regeneration temperature once the desorption time was shorter when the regeneration temperature was raised and the purge flowrate was the same for all the experiments. Additionally, the purge volume amount for any of experiments in *configuration 2* is much lower than that of the initial purge phase in *configuration 1* (0.64 $m^3.mol^{-1}$ CO_2 desorbed).

The values of energy per moles of CO_2 desorbed in Table 19 were estimated according to the following equation:

$$E_{He} = \frac{n_{He} \int_{T_{ads}}^{T_{reg}} C_{pg,He}\, dT}{moles\ of\ CO_2 desorbed} \tag{57}$$

where E_{He} is the energy required to increase the purge stream temperature from the adsorption temperature (T_{ads}) to the regeneration temperature (T_{reg}), n_{He} represents the number of moles of He employed during the time the desorption phase with heating was performed and $C_{p,He}$ is the specific molar calorific capacity of He. The volume purge amount was obtained simply multiplying the volumetric flow of the purge by the desorption time.

Equally important is to contemplate the actual scenario where the TSA separation process would operate, namely the availability of waste energy sources that could eventually be recycled for heating during regeneration. Clearly, the potential use of cheaper energy sources available at the power plant in order to counterbalance the energy requirements for CO_2 capture is currently a challenge for researchers on this area [48]. All in all, selecting an optimum TSA configuration for CO_2 capture is not a straightforward task once many trade-offs are encountered which confirms the necessity of a deeper study considering an economic analyses based on a real power plant scenario.

In regard to desorption simulations, once *configuration 1* was discarded for aforementioned reasons and *configuration 2* was considered as a potential TSA regeneration strategy to be coupled with adsorption step, experimental desorption isotherms were necessary to be performed once the adsorption isotherms applied merely to a 25-75 °C range and a wider temperature range was employed for desorption experiments. Correspondingly, desorption isotherms were carried out at 50 °C and 150 °C. In this case, moderate regeneration temperatures were preferred; this is why 300 °C was not included. The isotherm modeling was accomplished by means of traditional Dual-Site Langmuir (DSL) version (equation (58)) since the DSL version employed for breakthrough simulations failed to appropriately match the experimental data for CO_2.

$$q_{ei} = \frac{q_{maxi(1)} b_{i(1)} P_i}{1 + \sum_{i=1}^{NoC} b_{i(1)} P_i} + \frac{q_{maxi(2)} b_{i(2)} P_i}{1 + \sum_{i=1}^{NoC} b_{i(2)} P_i} \quad (58)$$

where $q_{maxi(j)}$ and $b_{i(j)}$ are the DSL isotherm parameters and P_i is the partial pressure of component i. The DSL parameters varied with temperature and were calculated as reported elsewhere [75]. It is worth to highlight that regardless the type of isotherm model used for the simulation, in essence, the best agreement between the model and the experimental data is vital in order to obtain the highest accuracy possible in the prediction. For that reason, during the course of this research, some adjustments were set on this issue particularly. For the case of N_2, no adjustment was necessary with respect to the isotherm modeling given its very low adsorbed amount.

The experimental desorption isotherms at 50 and 150°C and fittings by traditional DSL model for CO_2 on zeolite 13X are presented in Figure 36. The DSL model fitting fairly reproduced the experimental data with some mismatches at high pressures. Once the experiments are performed at the low-pressure range, the model fitting is considered appropriate for simulation purposes.

All things considered, desorption simulations were therefore focused on *configuration 2* and as an initial approach, a value of 125 °C was contemplated as regeneration temperature, being this value the lowest temperature tested in desorption experiments.

Figure 36. Pure CO_2 desorption isotherm at 50 °C (black) and at 150 °C (red) on zeolite 13X. Symbols represent experimental data; solid line represents DSL model fitting.

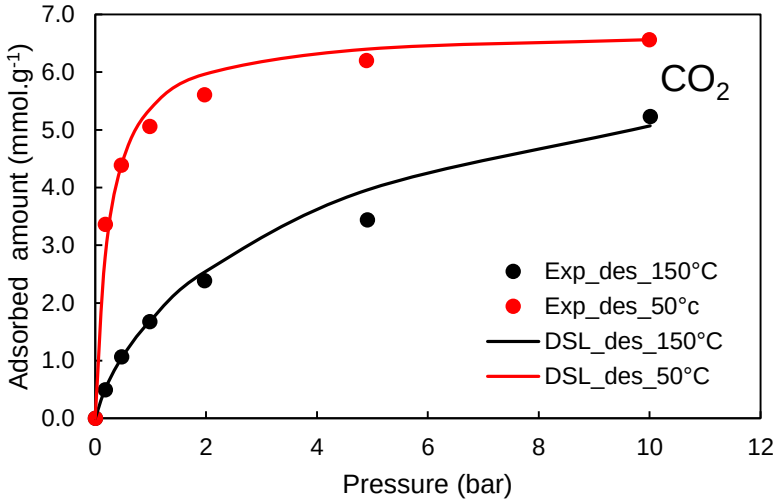

Source: own authorship.

Aside from the isotherm modeling, some other adjustments were mandatory for desorption simulation, namely some boundary and initial condition in the mass and energy balances described in the mathematical model formulation section:

- Mass balance boundary condition at *z=0*: once desorption phase starts, the CO_2 and N_2 supply is stopped, and only He is flowing through the bed. ($C_{g,CO_2}|_{inlet} = C_{g,N_2}|_{inlet} = 0|_{z=0}$).
- Energy balance initial condition: the surrounding temperature (T_{air}) changes with time by means of a temperature ramp of 20 °C/min up to the regeneration temperature ($T_{air}(t) = T_{regeneration}(t)$).
- The K_{LDF} values were also adjusted for the experimental desorption data. A value of 0.0075 s^{-1} and 0.0010 s^{-1} were found for CO_2 and N_2 respectively.

The rest of the equations, parameters and assumptions remained in the same way as in the breakthrough simulation.

The whole adsorption-desorption simulation process considering *configuration 2* as TSA regeneration strategy is shown in Figure 37.

Figure 37. Adsorption- desorption (*configuration 2*) process for CO_2-N_2 separation. Symbols represent experimental data and solid line represents simulated data.

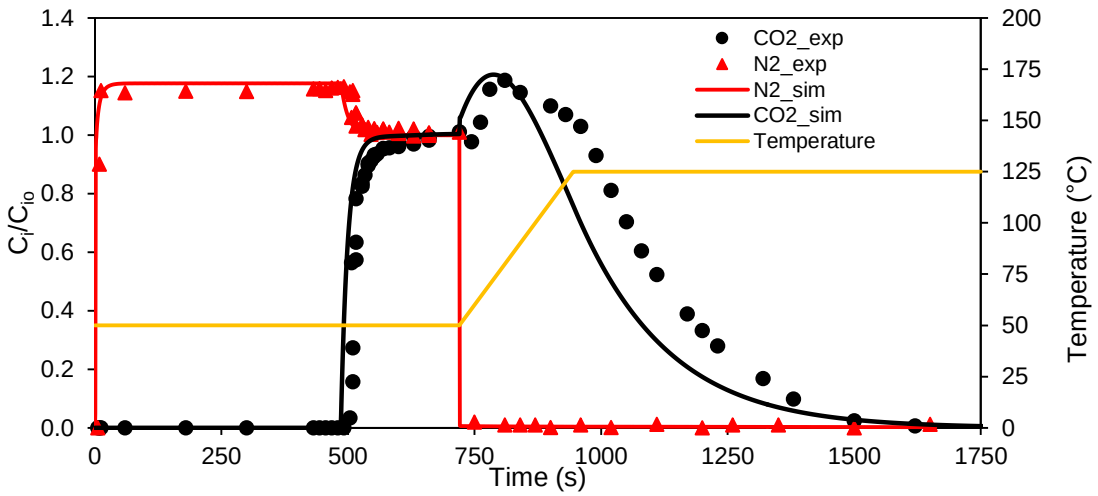

Source: own authorship

As can be noted, the desorption simulation for *configuration 2* is not fully successful since some inaccuracies are evident for CO_2 relative concentration profile, especially at the fall of the curve where an underestimation of the experimental data can be observed. These mismatches also led to an underestimation of the CO_2 recovery once the integration area of the desorption profile is reduced. In contrast, the final desorption time is well predicted, which would be convenient for adsorption-desorption synchronization. Furthermore, concerning synchronization, it is worth to clarify that although in real processes adsorption is usually ended at the break point of the strongly adsorbed species, for this research case, the discussion is based on completing adsorption step at the bed saturation point. As can been noted, if adsorption time is limited to the break point (ca 500 s), a reasonable loss in desorption recovery would happen once desorption time must be reduced to match the adsorption one. In summary, the efficiency of the separation process would be impaired significantly, not to mention that a cooling phase after desorption has not be considered nor experimentally evaluated for the whole process in this study.

In respect of the discrepancies exhibited in desorption simulations, the causes are not very clear but they may include experimental errors, inaccurate desorption isotherm modeling or inadequate mathematical model assumptions. The FBU is a hybrid experimental set-up, which is not automatic for the whole process methodology. The adsorption-desorption transition, namely the CO_2 and N_2 supply end and the He purge increase for desorption step are made manually by the manipulation of some valves and bottoms, which could eventually impair the experimental

results of the desorption phase specifically. Moreover, the proposed mathematical model is very sensitive to changes in the isotherm model i.e., a proper isotherm modeling is crucial to obtain good results in the prediction. Concerning the model assumptions, the most sensitive parameters to temperature fluctuations were varied with temperature, as previously addressed in the breakthrough simulation discussion, in order to prevent discrepancies arisen for this cause.

Figure 38. Adsorption- desorption (*configuration 2*) process for CO_2-N_2 separation with different purge flowrate. Symbols represent experimental data and solid line represent simulated data.

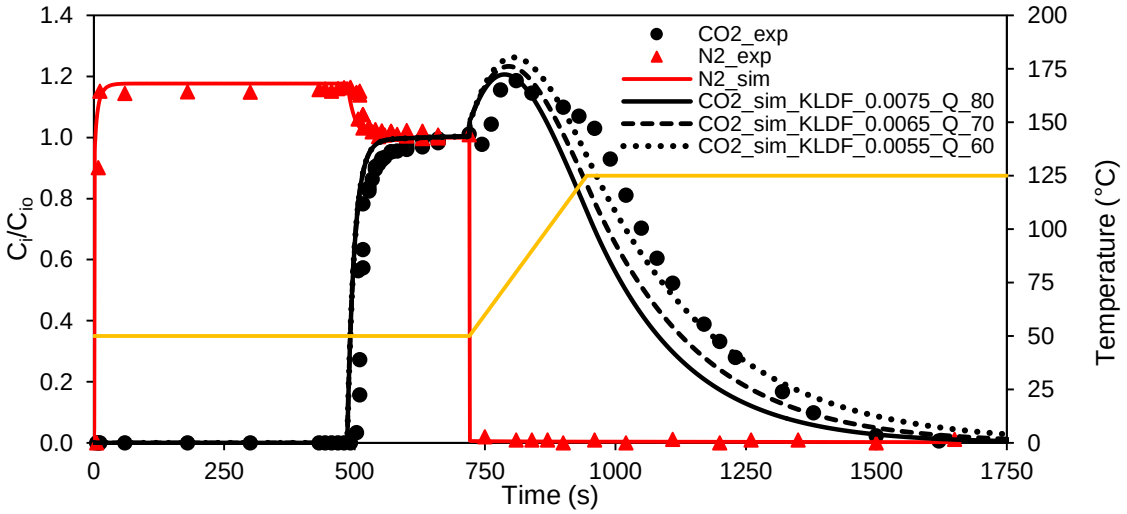

Source: own authorship

Consistent with above discussion, a parametric sensitivity analysis was conducted to try to identify causes or to understand the reasons of the inconsistencies between the simulated data and the experimental data. The variable that was more sensitive to shift the desorption curve was the purge flowrate. If one presume that the desorption phase was carried out with a He purge flowrate value lower than the established one (i.e., $Q=80\ cm^3min^{-1}\ STP$), the desorption process would slow down since the decrease of the CO_2 partial pressure would also be slower, so that the desorption curve would move more to the right. In Figure 38, one can observe that, when the He purge is diminished (e.g., for $Q= 70\ cm^3min^{-1}, 60\ cm^3min^{-1}\ STP$), the simulated data approach more closely to the experimental ones. This implies, in the same way, readjusting the value of K_{LDF} to values lower than the initially adjusted (Table 20) since otherwise the top of the curve would rise

with it. However, despite the good agreement obtained, it is just a supposition based on an eventual experimental fail.

Table 20. Readjusted K_{LDF} values for CO_2 at desorption for different purge flowrates.

$Q\ (cm^3 min^{-1})$	$K_{LDF}\ (s^{-1})$
70	0.0065
60	0.0055

Source: own authorship

6. CONCLUSION

Breakthrough-desorption experiments and simulations were carried out to assess two TSA configurations, with the aim of investigating the effect of purging and heating individually and altogether on the efficacy of CO_2-N_2 separation process, within a post-combustion scenario using commercial adsorbent zeolite 13X. All this with the intention of finding an adequate synchronization between the adsorption and desorption steps in a complete cycle. Based on the results obtained in this study, the following conclusions were derived:

- The CO_2-N_2 separation was possible by adsorption on material zeolite 13X. CO_2 is preferentially adsorbed on zeolite 13X in a fixed bed. The extent of selectivity of CO_2 over N_2 is more evident at dynamic conditions once CO_2 exhibited the same concentration profile in single and binary breakthrough curves, demonstrating that the presence of N_2 does not affect the CO_2 adsorption under this research conditions.
- Dual-Site Langmuir (DSL) model was the most suitable isotherm model from all the models tested in this study, once it prevented the appearance of numerical errors during the GPROMS iterative solution.
- TSA *configuration 1* regeneration strategy, which consisted of a purging phase initially and then both heating and purging, is likely to be unpractical for large-scale once the desorption time is too long in comparison with the adsorption time. In the same fashion, prolonged purging time leads to a low purity of the product recovered. However, this regeneration strategy exhibited a full CO_2 recovery regardless the regeneration temperature used in the experiments.
- TSA *configuration 2* regeneration strategy, which consisted of purging and heating at the same time, is likely to be coupled with the adsorption step given the desorption times obtained. The fact of omitting the initial inert purge step of *configuration 1* helped in the regeneration time reduction in *configuration 2*. Moderate temperatures, namely 125°C or 150°C are preferred for *configuration 2* to avoid high-energy penalties during the heating step. Despite that, further studies including economic evaluation are necessary to select an optimum outline for regeneration.
- Breakthrough simulations were able to reproduce the experimental data, validating the assumptions made on the proposed mathematical model for the adsorption phase. In

addition, accuracy of breakthrough simulations depends on a proper isotherm modeling. Despite the fact of considering non-adiabatic conditions on the mathematical model, adiabatic assumption tested on simulations showed no significant effect on the breakthrough profile.

- Desorption simulations required an isotherm modeling in a temperature range valid for the regeneration temperature to be evaluated. The desorption simulation profiles obtained exhibited some inconsistencies due to eventual experimental error, inadequate model assumption or inaccurate isotherm modeling. However, when assuming a lower value of the He purge during desorption, the simulated depletion profile matches much better the experimental data. In spite of the mismatches in the simulated desorption curve, the model was able to reproduce the total desorption time.

6.1. Suggestions for future work

Once *configuration 2* was considered appropriate for TSA in a post-combustion scenario and it did not exhibit 100% CO_2 recovery under the experiment conditions studied, experimental adsorption-desorption cycles are encouraged to be performed in order to evaluate the loss of adsorption capacity of the adsorbent after being exposed to numerous cycles. Consequently, a future work shall include simulations by a model able to provide information about the process variable behavior in cycles. The recovery, purity and also productivity and energy consumption estimation should be taken into account in a whole separation process assessment. Finally, the cooling step, which was not evaluated in this study, should be counted as part of the regeneration step after the heating-purging phase.

REFERENCES

1. FIGUEROA, J. D., *et al.* Advances in CO2 capture technology—The U.S. Department of Energy's Carbon Sequestration Program. **International Journal of Greenhouse Gas Control**, v. 2, n. 1, p. 9-20, 2008.
2. OLAJIRE, A. A. CO2 capture and separation technologies for end-of-pipe applications – A review. **Energy**, v. 35, n. 6, p. 2610-2628, 2010.
3. BEN-MANSOUR, R., *et al.* Carbon capture by physical adsorption: Materials, experimental investigations and numerical modeling and simulations – A review. **Applied Energy**, v. 161, p. 225-255, 2016.
4. LEUNG, D. Y. C., CARAMANNA, G., and MAROTO-VALER, M. M. An overview of current status of carbon dioxide capture and storage technologies. **Renewable and Sustainable Energy Reviews**, v. 39, p. 426-443, 2014.
5. DAVIDSON, O., *et al.* **IPCC Special Report on Carbon Dioxide Capture and Storage**. New York, 2005. 442 p.
6. BHOWN, A. S. and FREEMAN, B. C. Analysis and status of post-combustion carbon dioxide capture technologies. **Environ Sci Technol**, v. 45, n. 20, p. 8624-32, 2011.
7. MONDAL, M. K., BALSORA, H. K., and VARSHNEY, P. Progress and trends in CO2 capture/separation technologies: A review. **Energy**, v. 46, n. 1, p. 431-441, 2012.
8. JANSEN, D., *et al.* Pre-combustion CO2 capture. **International Journal of Greenhouse Gas Control**, v. 40, p. 167-187, 2015.
9. TAN, Y., *et al.* Property impacts on Carbon Capture and Storage (CCS) processes: A review. **Energy Conversion and Management**, v. 118, p. 204-222, 2016.
10. AMMENDOLA, P., RAGANATI, F., and CHIRONE, R. Effect of operating conditions on the CO2 recovery from a fine activated carbon by means of TSA in a fluidized bed assisted by acoustic fields. **Fuel Processing Technology**, v. 134, p. 494-501, 2015.
11. CHOI, S., DRESE, J. H., and JONES, C. W. Adsorbent materials for carbon dioxide capture from large anthropogenic point sources. **ChemSusChem**, v. 2, n. 9, p. 796-854, 2009.
12. CECILIA, J. A., *et al.* Functionalization of hollow silica microspheres by impregnation or grafted of amine groups for the CO2 capture. **International Journal of Greenhouse Gas Control**, v. 52, p. 344-356, 2016.

13. VILARRASA-GARCÍA, E., *et al.* Evaluation of porous clay heterostructures modified with amine species as adsorbent for the CO 2 capture. **Microporous and Mesoporous Materials**, v. 249, p. 25-33, 2017.
14. VILARRASA-GARCÍA, E., *et al.* Microwave-assisted nitric acid treatment of sepiolite. **Applied Surface Science**, v. 410, p. 315-325, 2017.
15. PHAM, T.-H., *et al.* Enhancement of CO2 capture by using synthesized nano-zeolite. **Journal of the Taiwan Institute of Chemical Engineers**, v. 64, p. 220-226, 2016.
16. JIAO, J., *et al.* Improvement of adsorbent materials for CO 2 capture by amine functionalized mesoporous silica with worm-hole framework structure. **Chemical Engineering Journal**, v. 306, p. 9-16, 2016.
17. CASTELLAZZI, P., *et al.* CO 2 capture by functionalized alumina sorbents: DiEthanolAmine on γ-alumina. **Microporous and Mesoporous Materials**, v. 226, p. 444-453, 2016.
18. MADDEN, D. and CURTIN, T. Carbon dioxide capture with amino-functionalised zeolite-β: A temperature programmed desorption study under dry and humid conditions. **Microporous and Mesoporous Materials**, v. 228, p. 310-317, 2016.
19. KO, D., *et al.* Analysis of purge gas temperature in cyclic TSA process **Chemical Engineering Science**, v. 57, p. 179-195, 2002.
20. ROUQUEROL, F., *et al.* **Adsorption by Powders and Porous Solids**. London: Academic Pres, 2014.
21. THOMMES, M., *et al.* Physisorption of gases, with special reference to the evaluation of surface area and pore size distribution (IUPAC Technical Report). **Pure and Applied Chemistry**, v. 87, p. 1051-1069, 2015.
22. LOWELL, S., *et al.* **Characterization of porous solids and powders: Surface area, porosity and density (Particle technology series)**. The Netherlands: Springer, 2006.
23. KUNDU, S. and GUPTA, A. K. Arsenic adsorption onto iron oxide-coated cement (IOCC): Regression analysis of equilibrium data with several isotherm models and their optimization. **Chemical Engineering Journal**, v. 122, n. 1-2, p. 93-106, 2006.
24. MALEK, A. and FAROOQ, S. Comparison of isotherm models for hydrocarbon adsorption on activated carbon. **AIChE Journal**, v. 42, n. 11, p. 3191-3201, 1996.

25. PERA-TITUS, M. On an isotherm thermodynamically consistent in Henry's region for describing gas adsorption in microporous materials. **J Colloid Interface Sci**, v. 345, n. 2, p. 410-6, 2010.
26. FOO, K. Y. and HAMEED, B. H. Insights into the modeling of adsorption isotherm systems. **Chemical Engineering Journal**, v. 156, n. 1, p. 2-10, 2010.
27. LANGMUIR, I. The constitution and fundamental properties of solids and liquids. **American Chemical Society**, v. 38, n. 11, p. 2221-2295, 1916.
28. FREUNDLICH, H. M. F. Over the adsorption in solution. **Phys. Chem.**, v. 57, p. 385-471, 1906.
29. SIPS, R. Combined form of Langmuir and Freundlich equations. **Chem. Phys.**, v. 16, p. 385-471, 1948.
30. TOTH, J. State equations of the solid gas interface layer. **Acta Chem. Acad. Hung.**, v. 69, p. 311-317, 1971.
31. HAGHSERESHT, F. and LU, Q. G. Adsorption Characteristics of Phenolic Compounds onto Coal-Reject Derived Adsorbents. **Energy & Fuels**, v. 12, n. 6, p. 1100-1107, 1998.
32. ADAMSON, A. W. and GAST, A. P. **Physical Chemistry of Surfaces**. New York: Wiley-Interscience, 1997.
33. GUNAY, A., ARSLANKAYA, E., and TOSUN, I. Lead removal from aqueous solution by natural and pretreated clinoptilolite: adsorption equilibrium and kinetics. **J Hazard Mater**, v. 146, n. 1-2, p. 362-71, 2007.
34. HO, Y. S., PORTER, J. F., and MCKAY, G. Equilibrium isotherm studies for the sorption of divalent metal ions onto peat: Copper, nickel, and lead single component systems. **Water, Air and Soil pollution**, v. 141, p. 1-33, 2002.
35. SONGOLZADEH, M., RAVANCHI, M. T., and SOLEIMANI, M. Carbon Dioxide Capture and Storage: A general review on adsorbents. **International Journal of Chemical, Molecular, Nuclear, Materials and Metallurgical Engineering**, v. 6, n. 10, p. 900-907, 2012.
36. HEDIN, N., *et al.* Adsorbents for the post-combustion capture of CO2 using rapid temperature swing or vacuum swing adsorption. **Applied Energy**, v. 104, p. 418-433, 2013.
37. CHESTER, A. W. and DEROUANE, E. G. **Zeolite Characterization and Catalysis, A tutorial.** Springer, 2009.

38. RUTHVEN, D. M. **Principles of Adsorption and Adsorption Processes**. New York: John Wiley & Sons, 1984.

39. ZHOU, K., CHAEMCHUEN, S., and VERPOORT, F. Alternative materials in technologies for Biogas upgrading via CO2 capture. **Renewable and Sustainable Energy Reviews**, v. 79, p. 1414-1441, 2017.

40. SAMANTA, A., *et al.* Post-Combustion CO2 Capture Using Solid Sorbents: A Review. **Industrial & Engineering Chemistry Research**, v. 51, n. 4, p. 1438-1463, 2011.

41. HARLICK, P. J. E. and TEZEL, F. H. An experimental adsorbent screening study for CO2 removal from N2. **Microporous and Mesoporous Materials**, v. 76, n. 1-3, p. 71-79, 2004.

42. BAHAMON, D. and VEGA, L. F. Systematic evaluation of materials for post-combustion CO2 capture in a Temperature Swing Adsorption process. **Chemical Engineering Journal**, v. 284, p. 438-447, 2016.

43. LI, G., *et al.* Dual mode roll-up effect in multicomponent non-isothermal adsorption processes with multilayered bed packing. **Chemical Engineering Science**, v. 66, n. 9, p. 1825-1834, 2011.

44. SEADER, J. D., HENLEY, E. J., and ROPER, D. K. **Separation Process Principles: Chemical and Biochemical Operations.** John Wiley & Sons, Inc, 2006.

45. LI, G., *et al.* Capture of CO2 from high humidity flue gas by vacuum swing adsorption with zeolite 13X. **Adsorption**, v. 14, n. 2-3, p. 415-422, 2008.

46. TLILI, N., GRÉVILLOT, G., and VALLIÈRES, C. Carbon dioxide capture and recovery by means of TSA and/or VSA. **International Journal of Greenhouse Gas Control**, v. 3, n. 5, p. 519-527, 2009.

47. CLAUSSE, M., MEREL, J., and MEUNIER, F. Numerical parametric study on CO2 capture by indirect thermal swing adsorption. **International Journal of Greenhouse Gas Control**, v. 5, n. 5, p. 1206-1213, 2011.

48. NTIAMOAH, A., *et al.* CO2 Capture by Temperature Swing Adsorption: Use of Hot CO2-Rich Gas for Regeneration. **Industrial & Engineering Chemistry Research**, v. 55, n. 3, p. 703-713, 2016.

49. RIBEIRO, R. P. P. L. **Electric Swing Adsorption for Gas Separation and Purification**. 2013. Thesis (Doctor in Chemical and Biological Engineering). Department of Chemical Engineering, University of Porto. 2013.

50. RAGANATI, F., AMMENDOLA, P., and CHIRONE, R. On improving the CO2 recovery efficiency of a conventional TSA process in a sound assisted fluidized bed by separating heating and purging. **Separation and Purification Technology**, v. 167, p. 24-31, 2016.

51. WANG, L., *et al.* Experimental and modeling investigation on post-combustion carbon dioxide capture using zeolite 13X-APG by hybrid VTSA process. **Chemical Engineering Journal**, v. 197, p. 151-161, 2012.

52. SONG, C., *et al.* Reducing energy consumption of advanced PTSA CO2 capture process—Experimental and numerical study. **Journal of the Taiwan Institute of Chemical Engineers**, v. 64, p. 69-78, 2016.

53. SHAFEEYAN, M. S., WAN DAUD, W. M. A., and SHAMIRI, A. A review of mathematical modeling of fixed-bed columns for carbon dioxide adsorption. **Chemical Engineering Research and Design**, v. 92, n. 5, p. 961-988, 2014.

54. DANTAS, T. L. P., *et al.* Modeling of the fixed-bed adsorption of carbon dioxide and a carbon dioxide-nitrogen mixture on zeolite 13X. **Brazilian Journal of Chemical Engineering**, v. 28, n. 3, p. 533-544, 2011.

55. RIOS, R. B., *et al.* Evaluation of carbon dioxide-nitrogen separation through fixed bed measurements and simulations. **Adsorption-Journal of the International Adsorption Society**, v. 20, n. 8, p. 945-957, 2014.

56. BEN-MANSOUR, R. and QASEM, N. A. A. An efficient temperature swing adsorption (TSA) process for separating CO2 from CO2 /N2 mixture using Mg-MOF-74. **Energy Conversion and Management**, v. 156, p. 10-24, 2018.

57. DANTAS, T. L. P., *et al.* Carbon dioxide–nitrogen separation through adsorption on activated carbon in a fixed bed. **Chemical Engineering Journal**, v. 169, n. 1-3, p. 11-19, 2011.

58. DREISBACH, F., SEIF, R., and LOSCH, H. W. Adsorption equilibria of CO/H-2 with a magnetic suspension balance - Purely gravimetric measurement. **Journal of Thermal Analysis and Calorimetry**, v. 71, n. 1, p. 73-82, 2003.

59. RIOS, R. **Avaliação da separação CO2-N2 para fins de captura através de medidas em leito fixo e de simulações**. 2015. Tese (Doutor em Engenharia Química). Departamento de Engenharia Química, Universidade Federal do Ceará. 2015.

60. BAE, T.-H., *et al.* Evaluation of cation-exchanged zeolite adsorbents for post-combustion carbon dioxide capture. **Energy Environ. Sci.**, v. 6, n. 1, p. 128-138, 2013.

61. SILVA, J. A. C., *et al.* Binary adsorption of CO2/CH4 in binderless beads of 13X zeolite. **Microporous and Mesoporous Materials**, v. 187, p. 100-107, 2014.

62. BASTOS-NETO, M. **Hydrogen purification and Storage by Adsorption in Porous Materials**. 2011. Thesis (Doctor Rerum Naturalium). Der Fakultät für Chemie und Mineralogie, Universität Leipzig. 2011.

63. CLAUSSE, M., BONJOUR, J., and MEUNIER, F. Adsorption of gas mixtures in TSA adsorbers under various heat removal conditions. **Chemical Engineering Science**, v. 59, n. 17, p. 3657-3670, 2004.

64. PERRY, R. H., GREEN, D. W., and MALONEY, J. O. **Perry's Chemical Engineers' Handbook** New York: McGraw-Hill, 1997.

65. BIRD, R. B., STEWART, W. E., and LIGHTFOOT, E. N. **Transport Phenomena**. New York: Wiley International, 2006.

66. SILVA, F. A. and RODRIGUES, A. Vacuum Swing Adsorption for Propylene/Propane Separation with 4A Zeolite. **Ind. Eng. Chem. Res.**, v. 40, n. 24, p. 5758-5774, 2001.

67. INCROPERA, F. P., *et al.* **Fundamentals of Heat and Mass Transfer**. John Wiley & Sons, 2011.

68. SIRIWARDANE, R. V., SHEN, M. S., and FISHER, E. P. Adsorption of CO2 on zeolites at moderate temperatures. **Energy & Fuels**, v. 19, n. 3, p. 1153-1159, 2005.

69. PARK, Y., *et al.* Adsorption equilibria and kinetics of six pure gases on pelletized zeolite 13X up to 1.0 MPa: CO2 , CO, N2 , CH4 , Ar and H2. **Chemical Engineering Journal**, v. 292, p. 348-365, 2016.

70. SIQUEIRA, R. M., *et al.* Carbon Dioxide Capture by Pressure Swing Adsorption. **Energy Procedia**, v. 114, p. 2182-2192, 2017.

71. DO, D. D. **Adsorption Analysis: Equilibria and Kinetics**. London: Imperial College Press, 1998.

72. COUCK, S., *et al.* 3D-printed SAPO-34 monoliths for gas separation. **Microporous and Mesoporous Materials**, v. 255, p. 185-191, 2018.

73. WEBLEY, P. A., *et al.* A New Multi-bed Vacuum Swing Adsorption Cycle for CO2 Capture from Flue Gas Streams. **Energy Procedia**, v. 114, p. 2467-2480, 2017.

74. CLAUSSE, M. **Étude d'un procédé d'adsorption TSA (Temperature Swing Adsorption) à chauffage et refroidissement indirects**. 2003. Thèse (Docteur). Conservatoire National des Arts et Metiers-CNAM. 2003.

75. NIKOLAIDIS, G. N., KIKKINIDES, E. S., and GEORGIADIS, M. C. A model-based approach for the evaluation of new zeolite 13X-based adsorbents for the efficient post-combustion CO 2 capture using P/VSA processes. **Chemical Engineering Research and Design**, v. 131, p. 362-374, 2018.